

pubs.acs.org/cm Article

Solution Aggregate Structures of Donor Polymers Determine the Morphology and Processing Resiliency of Non-Fullerene Organic Solar Cells

Azzaya Khasbaatar, Andrew Cheng, Austin L. Jones, Justin J. Kwok, Sang Kyu Park, Jessica K. Komar, Oliver Lin, Nicholas E. Jackson, Qian Chen, Dean M. DeLongchamp, John R. Reynolds, and Ying Diao*



Cite This: Chem. Mater. 2023, 35, 2713–2729



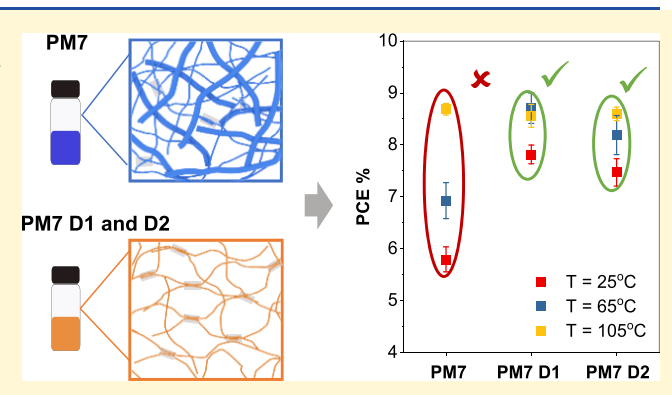
ACCESS I

III Metrics & More

Article Recommendations

s Supporting Information

ABSTRACT: The solution-state aggregation of conjugated polymers is critical to the morphology and device performance of bulk heterojunction (BHJ) organic solar cells (OSCs). However, the detailed structures of polymer solution-state aggregates and their impact on the morphology and device performance of OSCs remain largely unexplored. Herein, we utilize a benzodithiophene-based donor polymer (PM7) and its ester-functionalized derivatives (PM7 D1 and D2) with reduced backbone rigidity as our model systems to demonstrate how a polymer solution-state aggregate structure impacts the morphology and processing resiliency of OSCs. Using X-ray scattering and microscopic imaging techniques, we ascertain that PM7 solution forms a combination of semi-crystalline fiber aggregates and amorphous



polymer chain network aggregates, whereas PM7 D1 and D2 solutions primarily form amorphous network aggregates through sidechain associations. Interestingly, when the solution temperature is increased, the fiber aggregates of PM7 break down while the polymer network aggregates remain stable. Due to this temperature-dependent behavior of the fiber aggregates, blade-coated devices fabricated from the PM7 donor polymer and non-fullerene acceptor, ITIC-4F, lead to highly processing temperature-sensitive performance, whereas PM7 D1 and D2 polymers exhibit improved processing temperature resiliency. More importantly, we report that amorphous, network-like aggregates are conducive to superior device performance in blade-coated OSCs owing to the formation of blend films with short π – π stacking distance, small domain spacing, and face-on preferred molecular orientation. In contrast, we find that fiber-like aggregates lead to large π – π stacking distance, large domain spacing, and isotropic molecular orientation in the blend film, which deteriorate the device performance.

■ INTRODUCTION

Organic photovoltaics have emerged as a promising renewable energy technology that can reduce the cost of solar cell production using solution-based processing methods as compared to silicon-based solar cells, which require energyintensive manufacturing.1 Owing to their light weight, flexibility, and transparency, OSCs can also be used in a variety of novel applications including smart windows and powering portable devices or internet of things (IoTs).3 Although the device performance of OSCs has now reached a promising 19% efficiency with a single-junction cell on a laboratory scale,4 the processing method for most highperformance materials has been limited to spin coating, which is incompatible with large-area production of OSCs. On the other hand, meniscus-guided coating or solution printing techniques not only are compatible with large-scale roll-to-roll manufacturing but also can minimize solution waste to as low as 5%.6 However, transferring from spin coating to large-scale compatible processes is often challenging as the BHJ OSC

morphology is sensitive to changes in the film-drying dynamics and transport processes. Territhermore, the BHJ morphology of OSCs is not only sensitive to the processing techniques but also dependent on processing parameters and environmental conditions, after the complicating the device optimization of OSCs. Currently, controlling the morphology of OSCs for optimal device performance remains a bottleneck, typically requiring time-consuming trial-and-error-based approaches to adjust numerous processing parameters for device optimization. Therefore, achieving high-performing OSCs that can maintain their morphology regardless of the processing

Received: July 19, 2022 Revised: March 15, 2023 Published: March 27, 2023





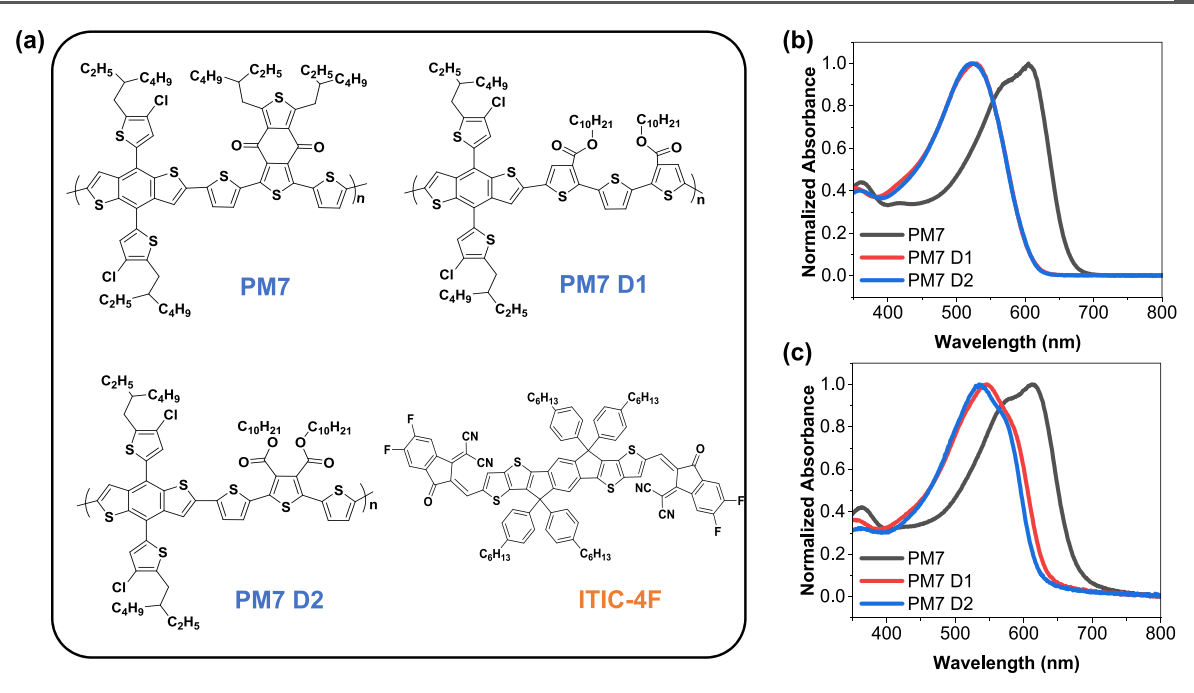


Figure 1. (a) PM7, PM7 D1, and PM7 D2 donor polymers (blue) and ITIC-4F acceptor molecule (orange) structures; (b) normalized UV-vis absorption spectroscopy of donor polymers in chlorobenzene (CB) solution at 20 mg/mL concentration; (c) normalized UV-vis absorption spectroscopy of neat polymer films blade coated from 20 mg/mL concentration of CB solutions.

parameters and environmental conditions is crucial for the successful commercialization of organic photovoltaics.

Recent studies have emphasized that solution-state aggregation of polymers is central to controlling the blend film morphology of OSCs, thereby potentially helping to overcome the aforementioned morphology control challenges. 14-16 For instance, a prominent work done by Qian et al. has shown that using a strongly aggregated solution of PBDTBDD for fabrication of OSCs yielded a superior device performance owing to the formation of nanoscale phase-separated domains, whereas using a thermally treated solution with reduced aggregation led to larger domains limiting charge generation and worsening the device performance.¹⁶ From the processing aspect, Hernandez et al. have shown that using an aggregated polymer solution leads to the same film morphology and device performance for both spin-coated and blade-coated OSCs as the morphology could be predetermined by the solution-state aggregation.¹⁴ In contrast, studies have also demonstrated that excessive aggregation of polymers in solution causes difficulty in processing 17 and leads to large crystalline domains, which are detrimental to charge generation.¹⁵ Recently, using polymers that exhibit temperature-dependent aggregation in solution partially resolved this issue as the strong solution-state aggregation of these polymers can be reduced by simply increasing the solution temperature before film deposition. 17 However, these temperature-dependent polymer aggregates have been reported to make the final morphology and device performance sensitive to processing parameters such as the spin coating rate, ¹⁷ thermal history of the solution, ¹⁶ solution temperature, ¹⁷ processing temperature, ^{10,11,18} and solution aging time. ¹⁹ On the other hand, more recently, Seo et al. reported that using a donor polymer with temperature-tolerant aggregation behavior improves processing temperature resiliency of OSCs.²⁰ Although these studies emphasize the importance of solution-state aggregation in controlling the morphology and processing resiliency of OSCs, detailed understanding of solution-state aggregates and their impact on the morphology and processing resiliency remains unclear. Therefore, the purpose of this study is to fill this knowledge gap by conducting a thorough investigation of polymer solution-state aggregation and its impact on the solidstate properties.

In this work, we investigate the solution-state aggregate structures of donor polymer PM7 and its ester-functionalized derivates PM7 D1 and D2, as shown in Figure 1a. Using smallangle X-ray scattering (SAXS), freeze-dried solution imaging, and optical spectroscopy, we find that PM7 generates a combination of fiber aggregates and amorphous network of polymer chains, whereas PM7 D1 and D2 solutions are primarily composed of amorphous network-like aggregates. Interestingly, we find that the fiber aggregates of PM7 are highly sensitive to the solution temperature, whereas the amorphous network-like aggregates remain stable. Furthermore, we report that these two types of aggregates lead to substantially different film morphologies and processing temperature resiliency in blade-coated non-fullerene-based OSCs. Specifically, temperature-tolerant network-like aggregates lead to superior device performance by forming favorable BHJ morphology with strong processing resiliency, whereas temperature-sensitive large fibrillar aggregates lead to inferior device performance and film morphologies, which are highly sensitive to the processing temperature.

■ RESULTS AND DISCUSSION

The repeat unit structures of the three donor polymers (PM7, PM7 D1, and PM7 D2) and the molecular acceptor (ITIC-4F) are presented in Figure 1a. The donor phase polymers have similar repeat unit structures with the only difference being the structure of the acceptor moiety in the main chain. In PM7, the highly fused benzodithiophenedione (BDD)-based acceptor moiety is incorporated, while for PM7 D1 and D2 polymers, this BDD-based moiety is replaced with an ester-functionalized

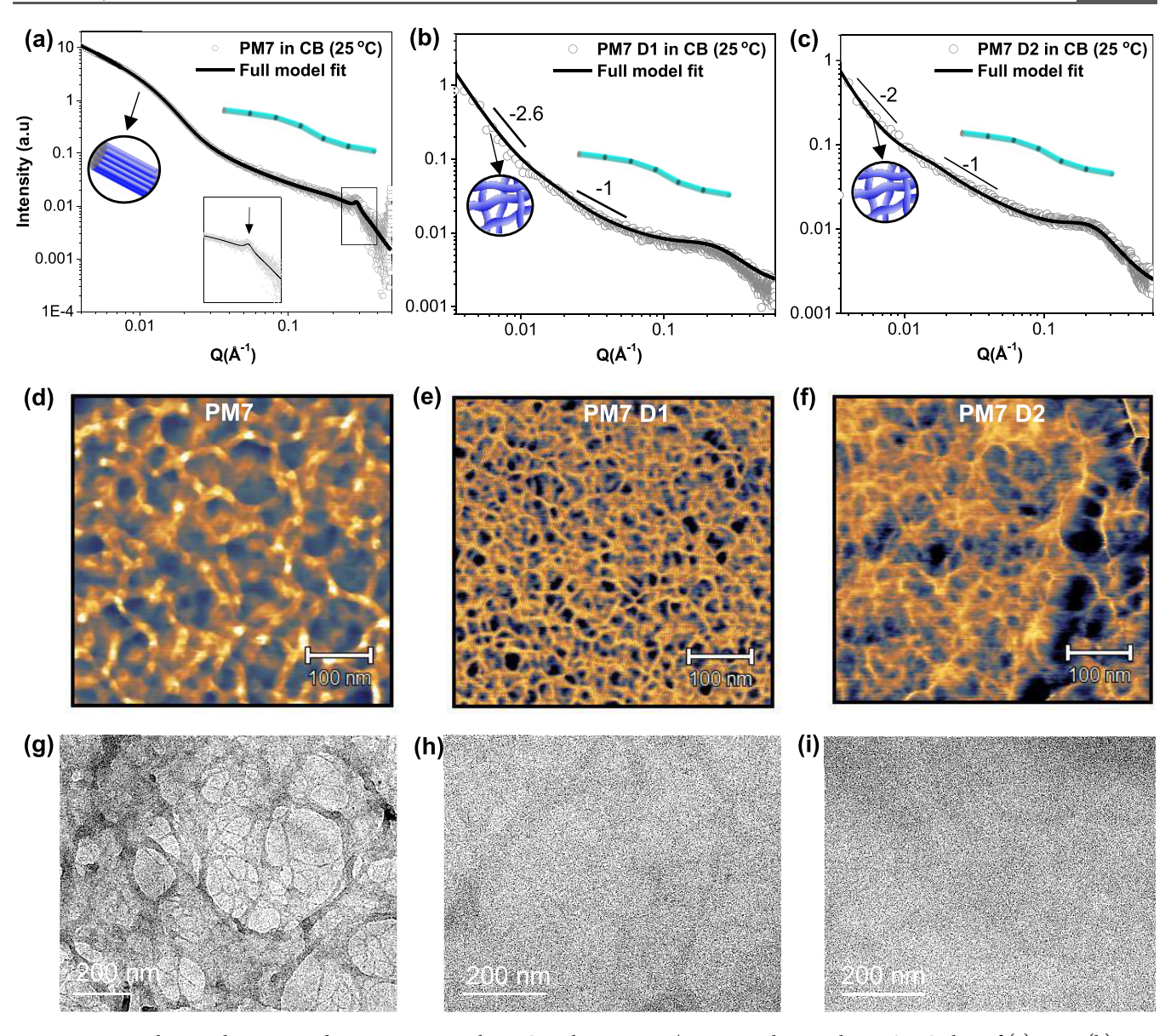


Figure 2. Neat polymer solution-state characterization results in CB solvent: 20 mg/mL neat polymer solution SAXS plots of (a) PM7, (b) PM7 D1, and (c) PM7 D2 conducted at 25 °C; AFM phase imaging of 20 mg/mL freeze-dried neat polymer solutions of (d) PM7, (e) PM7 D1, and (f) PM7 D2; TEM images for the 20 mg/mL freeze-dried neat polymer solutions of (g) PM7, (h) PM7 D1, and (i) PM7 D2.

terthiophene moiety, which leads to a wider optical bandgap. 21,22 The difference between the molecular structures of PM7 D1 and D2 is the location of ester group substitution; i.e., in PM7 D1, the two ester groups are located on the first and third thiophene units while in PM7 D2, they are both located on the central thiophene. Recently, Jones et al. showed that this structural modification reduced the required synthetic steps while still maintaining the device performance. Those authors have achieved the optimal device performance of 11.6, 12.1, and 9.9%, respectively, for spin-coated PM7, PM7 D1, and PM7 D2 when using ITIC-4F as the small-molecule acceptor.²³ Interestingly, the authors reported that this structural modification led to a more blue-shifted featureless UV-vis absorption in both PM7 D1 and D2 solutions as compared to PM7 solution, suggesting that the solution-state aggregation could be different. In this work, we will study the solution-state aggregation of these polymers in detail and investigate how different polymer aggregates impact the solidstate morphology and device properties of OSCs.

Determining the Polymer Solution-State Aggregate **Structures.** The neat polymer solutions (20 mg/mL concentration in chlorobenzene) were first investigated using UV-vis spectroscopy, as shown in Figure 1b. The UV-vis spectra of PM7 solution contains 0-0 and 0-1 vibronic peaks at 609 and 572 nm, respectively, indicating that the PM7 polymer backbone is highly ordered.^{24,25} On the other hand, PM7 D1 and D2 solutions both show blue-shifted absorption spectra without vibronic peaks suggesting increased backbone disorder with a shorter effective conjugation length.²⁴ Furthermore, the similarity of the solution and film UV-vis spectra of PM7 (Figure 1b,c) implies that PM7 may be strongly aggregated in solution. However, for highly rigid polymers, UV-vis cannot distinguish strongly aggregated solutions from highly rigid isolated polymers. 26 Therefore, solutions from highly rigid isolated polymers.26 we cannot rule out the possibility that PM7 solution is composed of highly rigid isolated polymers based on its UVvis spectra. On the other hand, the film UV-vis spectra of PM7 D1 and D2 become more red-shifted than their solution-

state UV-vis, and the 0-0 and 0-1 vibronic peaks start to emerge, indicating that the polymers become more planarized due to further aggregation from solution to the solid state. This indicates that PM7 D1 and D2 polymer backbones are more disordered in the solution state. Nevertheless, UV-vis spectroscopy measurements can only describe polymer backbone conformation and ordering and thus do not provide direct information regarding the solution-state aggregation of these polymers, let alone their detailed aggregate structures.

Therefore, we studied their solution-state aggregated structures using SAXS as well as directly imaging the aggregates by freeze-drying the solutions to complement SAXS results. Freeze-drying is an effective technique to transfer the solution-state properties to the solid state by freezing the solution-state aggregates in place. This method is extensively used to preserve protein drugs and vaccines as well as for preservation of biomaterials and cells in a dry form.²⁷ In the field of organic electronics, freeze-drying has also been previously utilized successfully to preserve the solution-state aggregation of polymers. ^{28–31} To preserve the solution-state aggregation, we use a liquid mixture of 63% propane and 37% ethane, which has a large heat capacity to rapidly freeze the sample and prevent crystallization during the cooling process.³² Shown in Figure 2a-c is the SAXS scattering profiles of each polymer solution along with their total model fitting, which will be discussed later. As presented in Figure 2a, the scattering profile for PM7 solution exhibits two Guinier knee regions around 0.01 and 0.3 Å⁻¹ which correspond to the cross sections of large fiber-like aggregates and single polymer chains in solution respectively, as we previously demonstrated in other conjugated polymer systems.³⁰ Atomic force microscopy (AFM) phase and transmission electron microscopy (TEM) images of the freeze-dried solution of PM7 confirm the existence of the fiber aggregates, as shown in Figure 2d,g (AFM height images are provided in Figure S1). Based on the AFM phase imaging, an average fiber radius of 9.5 ± 2.5 nm was determined, which is consistent with the radius of 11.5 ± 0.1 nm obtained from model fitting, as we discuss later. This consistency between the freeze-dried samples and SAXS measurements indicates that the solutionstate aggregate structures are maintained during freeze-drying. Furthermore, at a high Q region ($\approx 0.3 \text{ Å}^{-1}$), we observe a crystalline lamellar peak ($d_{lamellar} = 2.2$ nm), indicated by an arrow in the inset plot of Figure 2a, suggesting that these fiber aggregates are semi-crystalline. We also find that the fibers exhibit $\pi - \pi$ stacking ($d_{\pi - \pi} = 3.65 \text{ Å}$) using solution wide-angle X-ray scattering (WAXS) measurement (Figure S2). In addition to the fiber aggregates, the scattering profile of PM7 solution suggests that there are polymer chains, which adopt rigid rod-like conformation, as evidenced by the intermediate Q region $(0.03-0.3 \text{ Å}^{-1})$ with a Porod slope of -1 (Figure 2a).

In stark contrast to PM7, the scattering profiles for PM7 D1 and D2 solutions (Figure 2b,c) do not possess a Guinier knee corresponding to large fiber aggregates in the Q region accessible for SAXS. Instead, we observe two Porod regions with a slope between -2 and -3 at low Q, a slope of -1 at intermediate Q, and a broad structure factor peak attributed to lamellar stacking 33,34 at high Q for both PM7 D1 and D2 solutions. The Porod slope of -1, as previously mentioned for PM7 solution, corresponds to rigid rod-like polymer chains or chain segments, whereas power law slopes between -2 and -3 at the low Q region indicate that there might be large-scale aggregates in these solutions beyond the Q region accessible

for SAXS ($Q \ge 0.004 \text{ Å}^{-1}$ or length scale $\ge 150 \text{ nm}$). However, we find that TEM imaging of the freeze-dried solutions for PM7 D1 and D2 is mainly featureless, suggesting that no largescale aggregates exist beyond ≈150 nm (Figure 2h,i). Interestingly, based on AFM phase imaging (Figure 2e,f), we notice network-like aggregates in PM7 D1 and D2 freeze-dried samples composed of single polymer chains as the width of these features is less than ≈ 5 nm (the exact width cannot be determined precisely since AFM resolution is limited by the AFM tip radius of 2-5 nm). It has been previously demonstrated that network or fractal-like structures exhibit power law slopes between -2 and -3, corresponding to the mass fractal of these aggregates, 35,36 which appears to be consistent with our results. Alternatively, such power law slopes at low Q can also be caused by excess scattering due to concentration fluctuations known as Picot and Benoit scattering.³⁷ However, we excluded this possibility as excess scattering due to concentration fluctuations is highly sensitive to the solution preparation method and temperature of the solution,³⁷ while the low Q scattering features we observe are not sensitive to these factors. For instance, we re-measured PM7 D2 solution using SAXS after preparing the solution by thermally annealing the solution at 100 °C and then stirring the solution at 25 °C overnight and observed that the power law region at low Q is still maintained (Figure S3). Furthermore, the structure factor peaks at the high Q region indicate that the polymer chains are associated, rather than existing as dispersed polymer chains in the solution.

To further explain the origin of network-like aggregates, we compare the SAXS profile of PM7 D2 solution in CB with the scattering of PM7 D2 solution prepared in chloronaphthalene (CN) since CN solution exhibits a more pronounced power law region at low Q, as shown in Figure S4a. We find that CN is a better solvent for PM7 D2 than CB, evident from its more blue-shifted UV-vis spectra (Figure S4b). Due to this improved solvent quality, the intensity of the intermediate Q region corresponding to rigid polymer chains in CN is substantially reduced than in CB. Although polymer backbone becomes well-dissolved in CN, the power law region at low Q corresponding to the network-like structure is maintained and the broad structure factor peak at high Q in CN solution becomes more pronounced. We believe that in CN solution, the network aggregates are formed by well-solubilized polymer chains, forming an amorphous network-like structure likely through sidechain interactions, leading to the broad structure factor peak observed at high Q.28 Similarly for CB solution, we attribute the power law region at low Q to the scattering from the network-like aggregates. However, different from CN, CB solution has a more intense intermediate Porod region corresponding to a larger number of rigid polymer chain segments, which is consistent with its decreased solvent quality. From WAXS measurements, we did not observe $\pi - \pi$ stacking as the intensity is quite low to overcome background scattering. However, using TEM electron diffraction measurements on the freeze-dried samples, we observe a coherence feature at 4.8 and 5 Å in PM7 D1 and D2 freeze-dried samples, respectively (Figure S5), corresponding to amorphous alkyl sidechain stacking distance.³⁸ This implies that PM7 D1 and D2 polymers form amorphous network-like aggregates via alkyl sidechain association, resulting in the broad lamellar stacking peak in their scattering profiles. We also note that the freezedried sample of PM7 exhibits alkyl sidechain stacking at 4.5 Å (Figure S5), slightly closer than those of PM7 D1 and D2,

likely due to the crystalline lamellar stacking of the fiber aggregates, forming closer sidechain interactions.

Based on the scattering features from SAXS plots and freezedried imaging of the neat polymer solutions, we have established that PM7 solution consists of two distinct populations, which are fiber aggregates and rigid rod-like polymer chains (which we will later show as part of a networklike aggregate), whereas PM7 D1 and D2 solutions are composed of network-like aggregates with rigid polymer segments. With this knowledge, we can proceed with fitting the scattering profiles to obtain quantitative information such as the size of aggregates and polymer chains. When fitting the SAXS profiles, using an appropriate model that accurately describes the system is critical since multiple models can produce equally good fits, leading to the lack of model uniqueness.³⁹ Obtaining some knowledge about the system by using complementary measurements thus ensures selecting a model that can capture the actual macromolecular structures in the solution state. For a multi-particulate system such as a polymer solution composed of fibers and single polymer chains, we have recently published a model fitting approach, which has successfully described similar donor-acceptor (D-A)-conjugated polymer solutions at various concentrations and solvents.³⁰ In this model, we describe the fiber aggregates and the polymer chains by using the flexible cylinder model, 40,41 which is commonly used for fitting the scattering profiles from semiflexible donor-acceptor-conjugated polymer systems. If there are network-like aggregates and lamellar stacking present in the solution, this model can be modified to include power law and pseudo-Voigt function to fit the scattering at low O and the lamellar structure factor peak at the high Q region, respectively.

For PM7 solution, we firstly fit the scattering plot to a combination of two flexible cylinder models (or 2FC model) to capture two different populations in the solution (fibers and polymer chains). When the 2FC model is used to fit the scattering profile of PM7 solution, we find that it does not fully capture the low and high Q regions (Figure S6a) and leads to a large chi-squared value of 5.2 and a large variation in the residuals (Figure S6b). We also find that this model gives an extremely small cylinder radius of 3.5 Å, which is not physically possible for polymers with long alkyl sidechains (eight carbon atoms). Considering that network-like aggregates lead to scattering at both low and high Q regions due to the dimensionality of the network and lamellar interactions as previously discussed, we hypothesize that PM7 solution contains polymer network aggregates in addition to fiber-like aggregates. We validated this inference using temperaturedependent SAXS shown later. To include the contribution from the network-like aggregates, we thus add power law and pseudo-Voigt peak functions to describe the dimensionality of the aggregate and the hidden broad lamellar structure factor peak originating from sidechain interactions within the network, respectively. This modified 2FC model shows an improved fit with a reduced chi-squared value of 2.2 and smaller variations in the residuals (Figure S7). To capture the lamellar stacking peak arising from the fibrillar aggregates, we added a Lorentz peak function to this modified 2FC model, which gives a chi-squared value of 1.9 and residuals, as shown in Figure S8. For PM7 D1 and D2 solutions, since there is no contribution from fiber aggregates, we removed one of the flexible cylinder contributions from the modified 2FC model. Using this approach, we obtained the final model fitting results

provided in Figure S9 and Table S3, which show the full details of the deconvolution of the model fits and the resulting fitting parameters, respectively.

When fitting the scattering profiles to a model with multiple parameters, parameter correlations need to be considered, especially when there is no adequate signal and the functions are overlapped. To avoid parameter correlations, we fix the parameters that can be estimated using other methods. For example, since there is no Guinier knee corresponding to the length of fibers and polymer chains for PM7, we fix the length parameter of the two flexible cylinder contributions (L_1 and L_2), which represent the polymer chain length and the fiber length, respectively, to 100 nm, which is close to the contour length of the polymer (Table S1). However, we expect that the polymer chain segments within the network-like aggregates would be smaller than this value. Additionally, since the Guinier knee from the cross section of polymer chains and pseudo-Voigt peak overlaps at high Q, we fix the polymer chain radius ($R_p = 1.5 \text{ nm}$) based on the radius obtained from model fitting results from PM7 D1 where we were able to see the pseudo-Voigt peak more clearly. Using this fitting procedure, we find that the cross-sectional radius of fiber aggregates of PM7 is $R_f = 11.4 \pm 0.07$ nm (error is the fitting error from the model), consistent with the average radius of 9.5 \pm 2.5 nm obtained from AFM imaging of the freeze-dried samples (Figure 2). Furthermore, all polymer solutions contain broad structure factor peaks corresponding to lamellar stacking distances within the network aggregates, as indicated in Table 1. These values are larger than the lamellar stacking distance of 1.9-2.2 nm observed in the blend films, as shown later from grazing incidence wide-angle X-ray scattering (GIWAXS), which could be due to the swelling of the lamella in the solution state. 42 We were also able to extract the length of the rigid polymer chain segments of PM7 D1 and D2 polymers and found that it is consistent with the length of

Table 1. Summary of Quantitative Details of the Solution State Aggregation

| parameters | PM7 (25 °C) | PM7 D1 (25 °C) | PM7 D2 (25 °C) |
|--|-------------------|-------------------|-------------------|
| length of polymer chain segment (nm) | 100 ^a | 30.3 ± 13.7 | 28.4 ± 3.9 |
| persistence length (nm) | $\gg R_p$ | 7.9 ± 3.0 | 10.3 ± 3.5 |
| polymer chain radius, $R_{\rm p}$ (nm) | 1.5 ^b | 1.5 ± 0.6 | 1.4 ± 0.3 |
| lamellar stacking distance within the network (nm) | 3.9 ± 0.7 | 3.4 ± 0.6 | 3.4 ± 0.4 |
| FWHM of lamellar stacking of the network (\mathring{A}^{-1}) | 0.28 ± 0.01 | 0.31 ± 0.02 | 0.28 ± 0.01 |
| fiber length (nm) | 100 ^a | | |
| fiber radius, $R_{\rm f}$ (nm) | 11.5 ± 0.1 | | |
| lamellar stacking distance within fibers (nm) | 2.16 ± 0.01 | | |
| FWHM of lamellar stacking of the fibers (\mathring{A}^{-1}) | 0.016 ± 0.001 | | |
| π– $π$ stacking distance (Å) | 3.65 ± 0.01 | | |

"Values were fixed during model fitting due to the absence of Guinier knee corresponding to the length at low Q. bValue was fixed based on the radius obtained from PM7 D1 due to function overlap of the Guinier knee of flexible cylinder and the pseudo-Voigt peak functions at high Q.

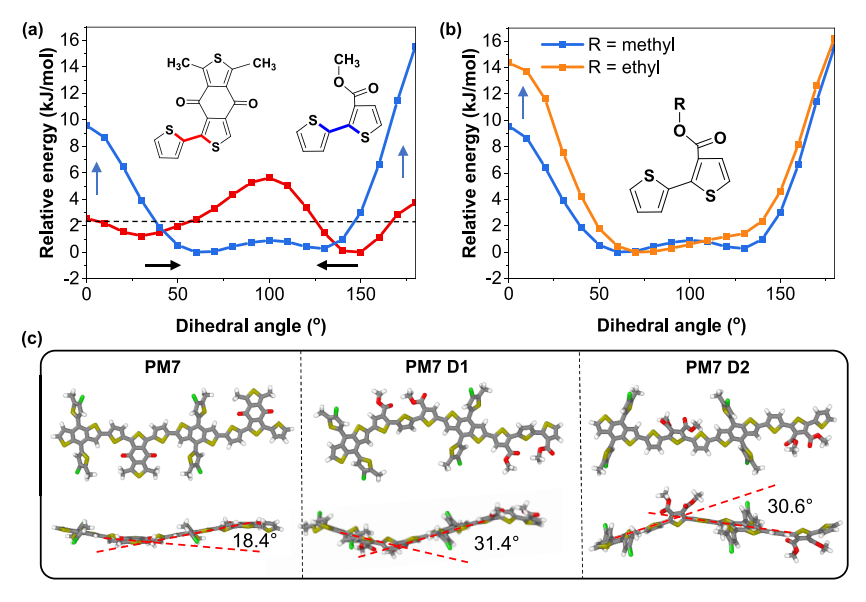


Figure 3. DFT calculation results for comparing the backbone conformation: (a) Potential energy scans for the dihedral angle between thiophene and BDD groups (thiophene-BDD) for PM7 (red) and the dihedral angle between thiophene and ester-substituted thiophene groups (thiophene-ester) for both PM7 D1 and D2 (blue); (b) comparison of potential energy scans for the thiophene and ester-thiophene dihedral of PM7 D1 and D2 when the sidechain is replaced from methyl to an ethyl group; (c) face (top) and side (bottom) view images of the optimized dimer conformations (anti) of the three polymers.

polymer segments obtained from AFM phase imaging of the freeze-dried solutions, as shown in Figure 2e,f (20–30 nm). The persistence lengths of these polymer chain segments are 7.9 and 10 nm, respectively, whereas for PM7, the persistence length could not be accurately determined due to the overshadowing Guinier knee from the fiber cross section, but it is expected to be significantly higher than the polymer chain radius ($l_p \gg R_p$). Nevertheless, we predict that PM7 is highly rigid due to its planar BDD and conformationally locked acceptor core, which has been shown to induce strong aggregation and backbone planarity in many polymer systems. ^{43,44}

To further investigate how BDD and ester-substituted thiophene groups affect polymer backbone conformation, we compared the potential energy scans of the dihedral angles corresponding to these groups by using DFT with the wB97xD method at the 6-31G (d, p) basis set. 45-48 This dispersioncorrected functional is a more accurate DFT method in estimating the torsional barrier and dihedral angles of conjugated molecules than the commonly used B3LYP functional, which overestimates the torsional barrier and overly stabilizes the planar conjugated conformations due to its many-electron self-interaction error. 48 In Figure 3a, the potential energy plots corresponding to the dihedral angle between thiophene and BDD groups (thiophene-BDD) of PM7 (red) and the dihedral angle between thiophene and ester-substituted thiophene groups (thiophene-ester) of both PM7 D1 and D2 (blue) are presented and show significantly different features. The fragments used for obtaining the potential energy plots are shown in the inset plot of Figure 3a. We focus our discussion on comparing these dihedral angles since the potential energy scans of dihedral angles between donor and acceptor moieties were found similar for PM7 and its derivatives (Figure S10). In Figure 3a, 0° on the horizontal axis refers to the anti-conformation in which sulfur atoms on the adjacent thiophene groups are facing the opposite directions while at 180° sulfur atoms are syn or on

the same side. Each plot indicates two local minima corresponding to the dihedral angles of anti and syn conformations. Since the energy difference between the local minima is close to 1 kT at room temperature for both plots as indicated by the dashed line in Figure 3a, there is no energetic preference between anti and syn conformations. Nevertheless, the minimum-energy dihedral angles of thiophene-ester groups of PM7 D1 and D2 are shifted toward the maximum dihedral angle of 90° as compared to the thiophene-BDD dihedrals of PM7 (indicated by arrows), suggesting that PM7 D1 and D2 exhibit larger dihedral angles than PM7 regardless of their conformation. Furthermore, by optimizing the dimers (anticonformations) of these molecules as shown in Figure 3c, we demonstrate that the large dihedral angles of PM7 D1 and D2 disrupt the backbone planarity of PM7. Specifically, from the side-view images of Figure 3a, we can clearly see that PM7 D1 and D2 dimers exhibit backbone twist angles of 31.4 and 30.6° respectively, while PM7 has a much lower backbone twist of 18.4°.

Another major difference between the potential energy plots is the energy barrier to planarize the dihedral angles, which indicates the likelihood of forming planar backbone (indicated by the blue arrows in Figure 3a). As shown in Figure 3a, the energy barriers required to planarize the dihedral angle between thiophene and ester-thiophene groups of PM7 D1 and D2 to 0 and 180° reach 9-10 and 13-16 kJ/mol, respectively, while the energy barriers to planarize the thiophene-BDD dihedral angle of PM7 are only around 2.5 and 3.5 kJ/mol (approximately 1 and 1.4 kT at room temperature). We attribute these high-energy barriers to planarize the ester-thiophene dihedral angle of PM7 D1 and D2 to the steric hindrance originating from the alkyl sidechain connected to the ester group. Indeed, when the methyl group is replaced with an ethyl group, the energy barriers to planarize this dihedral angle increase further as shown in Figure 3b, suggesting that alkyl sidechains induce strong steric hindrance, making it difficult to planarize the dihedral angle. On the other

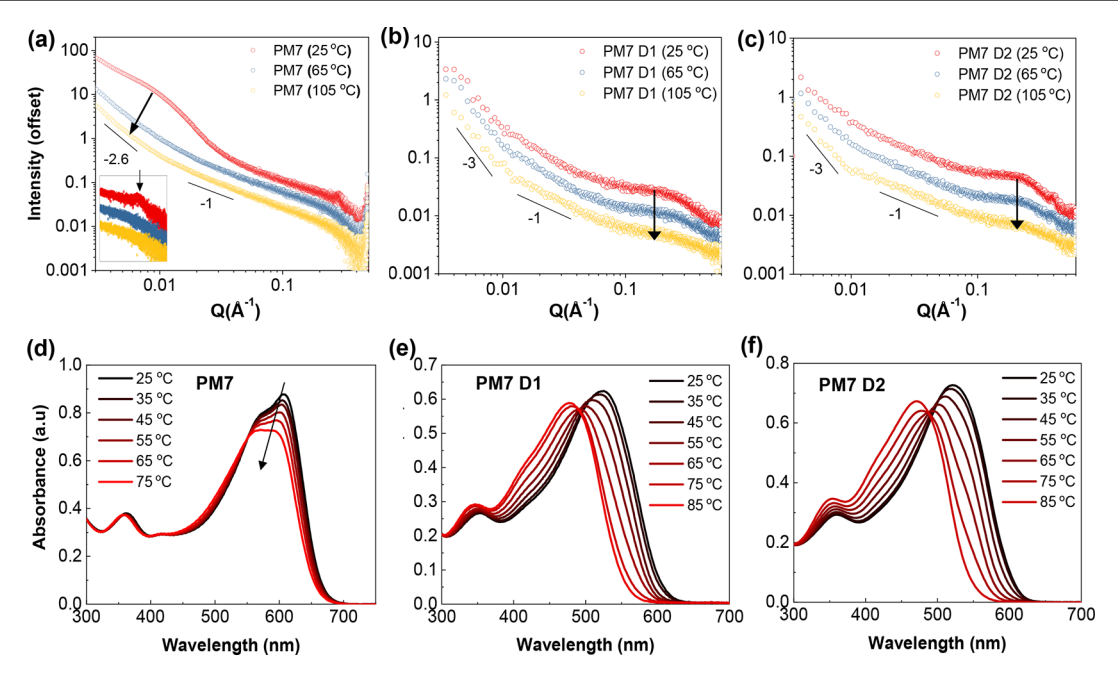


Figure 4. Temperature dependence of the neat polymer solutions. Temperature-dependent SAXS results for 20 mg/mL neat polymer solutions of (a) PM7, (b) PM7 D1, and (c) PM7 D2 (25 and 65 °C curves were shifted up by a multiplication of 4 and 2, respectively); temperature-dependent UV—vis for 20 mg/mL neat polymer solutions of (d) PM7, (e) PM7 D1, and (f) PM7 D2.

hand, for PM7, sidechains are substituted further from the adjacent thiophene unit likely causing less steric hindrance as compared to sidechains directly connected to the ester group in the case of PM7 D1 and D2. Moreover, we observe that the energy barrier between anti and syn conformations for the dihedral angle of PM7 D1 and D2 is lower than that for PM7 (Figure 3a), suggesting that PM7 D1 and D2 are not only more torsionally distorted from planarity and less likely to planarize but also more flexible than PM7. We note that the ester groups of PM7 D1 and D2 are rotationally flexible so the configuration where carbonyl (C=O) oxygen of ester group faces the thiophene group as shown in Figure S11 is also possible. However, regardless of this ester group configuration, we observe the same trend in the potential energy scans where PM7 D1 and D2 have larger minimum-energy dihedral angles, higher energy barriers to planarize, and lower energy barrier to switch from anti to syn conformation than PM7 (Figure S11).

Overall, our DFT results suggest that the planarity-disrupting ester-functionalized acceptor moieties make PM7 D1 and D2 more torsional and flexible than PM7, which could explain why they do not form fiber aggregates in solution but instead form an amorphous polymer chain network. We also note that PM7 D1 and D2 possess long unbranched alkyl sidechains, which could contribute to making them more solubilized by disrupting backbone interactions. On the other hand, the more rigid and planar PM7 polymer forms fiber aggregates via strong polymer chain interactions as evidenced by the lamellar and $\pi-\pi$ stacking interactions observed in the solution state.

Temperature Dependence of the Polymer Solution-State Aggregate Structures. The effect of solution temperature on the solution-state aggregation behavior was further investigated by using temperature-dependent SAXS and UV—vis spectroscopy. From the temperature-dependent SAXS solution experiment for PM7 (Figure 4a), we observe that the Guinier knee region, which corresponds to the cross section of the large fiber-like aggregates, completely disappears when the

solution temperature is increased. This led to revelation of the previously hidden Porod region at the low Q with a slope close to -2.6, attributed to the contribution from network-like aggregates. This indicates that the fibers are dissolved with increasing temperature, leading to a solution mainly composed of network-like aggregates. By fitting the SAXS profile for PM7 solution at 65 °C, we find that the length of the rigid chain segments is 26 ± 3.8 nm (Table S3), which is shorter than the contour length of the polymer chain (Table S1), indicating that the network aggregates are composed of the rigid chain segments. In addition to the dissolution of fibers, we observe that the sharp lamellar peak disappears with increasing temperature (inset plot in Figure 4a). We also found that the intensity of the π - π stacking peak at 105 °C became too low to overcome background scattering from WAXS measurement. These observations indicate that the lamellar and π – π interactions occur within the fiber aggregates in solution and disappear when the fibers are dissolved at high solution temperatures. The temperature-dependent solution UV-vis of PM7 (Figure 4d) also demonstrates that the vibronic fine structure decreases with increasing temperature, suggesting an increase in the backbone disorder. ^{49,50} On the other hand, the temperature-dependent SAXS profiles of PM7 D1 and D2 solutions (Figure 4b,c) only show a decrease in the intensity of the structure factor peak while the power law scattering at low Q remains, indicating that the amorphous network structure is still maintained. It is, however, notable that the intensity of the broad structure factor peak decreases more substantially in PM7 D1 and D2 than in PM7 and that the temperaturedependent UV-vis spectra indicate a more significant blue shift in PM7 D1 and D2 solutions than in PM7 with increasing temperature (Figure 4d,e). In addition to the blue shift, an isosbestic point is observed in both PM7 D1 and D2 solution UV-vis absorption. The blue-shifted UV-vis spectra indicate that PM7 D1 and D2 become more flexible due to further backbone twist,⁵¹ and the apparent isosbestic point suggests that polymer chains transition between anti and syn

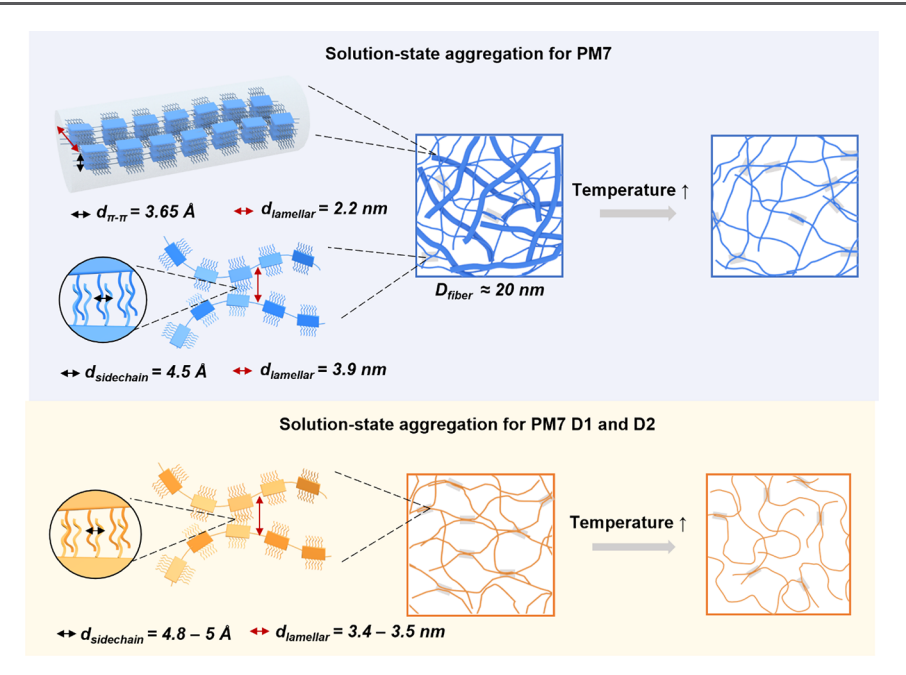


Figure 5. Proposed solution-state aggregated structure and temperature dependence of the three polymers: The top row shows the detailed structure of the fiber and network aggregates in PM7 solution and the temperature dependence of the solution-state aggregation with increasing temperatures. The bottom row represents the detailed structure for PM7 D1 and D2 aggregates in solution and their solution temperature dependence. The gray squares in the figure indicate sidechain associations within the network-like aggregates.

conformations, which is consistent with the low potential energy barrier determined from the DFT calculations (Figure 3a). We thus attribute the decrease in the intensity of the broad structure factor peak to the increased flexibility of PM7 D1 and D2 polymer chains, leading to fewer chain associations as the solution temperature rises. In PM7 solution, on the other hand, the polymer chains are expected to be highly rigid, thus requiring more thermal energy to make them more flexible and well-solubilized. Despite the rigid polymer chains of PM7, however, the semi-crystalline fiber aggregates are highly sensitive to temperature, leading to a substantial order-to-disorder transition whereas the amorphous network-like aggregates of PM7 D1 and D2 are maintained.

Based on the solution-state characterization results, we propose schematics for the polymer aggregate structures and their temperature dependence, as shown in Figure 5. The schematics indicate that PM7 solution contains semicrystalline fiber aggregates composed of lamellar and π - π stacking as well as network-like aggregates of polymer chains formed via alkyl sidechain associations. The fibrillar aggregates of PM7 dissolve at high solution temperatures, resulting in a solution mainly composed of the network-like aggregates. PM7 D1 and D2, on the other hand, form sidechain-associated network-like aggregates that can maintain their structures at high temperatures despite having fewer sidechain associations due to their increased chain flexibility. We hypothesize that this temperature resiliency of the network-like structures of PM7 D1 and D2 will make them more resilient to processing temperature during fabrication of OSCs.

Thus far, we have investigated the neat polymer solutionstate aggregate structures and their solution temperature dependence. However, BHJ-based OSCs are typically fabricated from a blend solution of donor and acceptor materials. Therefore, it is critical to determine whether the acceptor material influences the aggregate structures of donor polymers and their temperature dependence. Using SAXS on

blend solutions of the donor polymer and the small-molecule acceptor, ITIC-4F, we discovered that the presence of ITIC-4F has no effect on the solution-state aggregate structures of the donor polymers. Shown in Figure S12 are the scattering profiles of the blend solutions, which closely resemble the scattering profiles of the neat donor polymer solutions (Figure 2a-c). Furthermore, we also obtained the temperaturedependent UV-vis spectra of the blend solutions (Figure S13a-c) to investigate whether the temperature-dependent behavior of the donor polymer is altered by the presence of ITIC-4F. When the neat solution spectra of ITIC-4F (Figure S14) are subtracted from the blend solution UV-vis spectra, we obtain the temperature-dependent UV-vis spectra of only the donor polymers from the blend solutions (Figure S13d–f), which closely matches temperature-dependent UV-vis spectra of those from the neat polymer solution (Figure 4d-f). Based on these results, we conclude that the solution-state aggregation of donor polymers and their temperature-dependent behavior are not altered by the presence of small

Determining the Processing Conditions for Blade Coating. It is well known that carrying out active film formation by spin-coating under an inert atmosphere using 1,8diiodooctane (DIO) as an additive can provide high-performance solar cells, and the PM7:ITIC-4F pair has been reported to have a PCE up to 14%.⁵² In this work, we employed meniscus-guided coating in air without additives to demonstrate compatibility with scalable large-area coating techniques under more practical conditions. Unlike spin coating, in which the spin speed of the substrate is the only processing parameter, the blade coating process involves several processing parameters such as coating speed, substrate temperature, and blade angle, which all influence the film thickness, uniformity, and device performance of OSCs. The objective is to obtain uniform films with an optimal film thickness of around 80-100 nm under various substrate

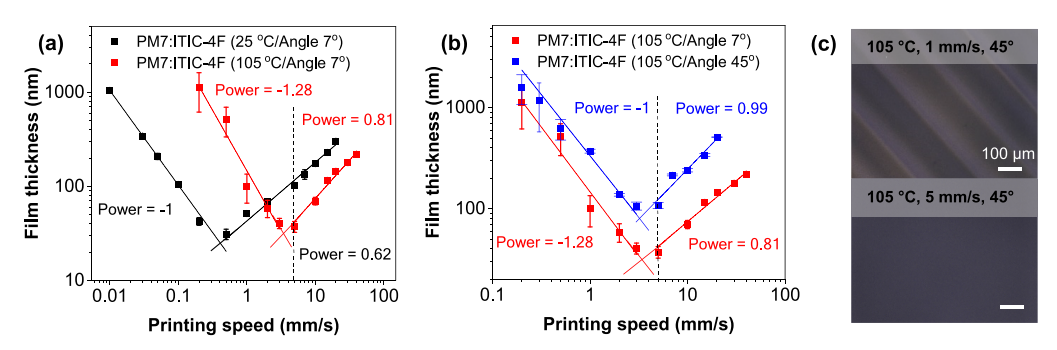


Figure 6. Film thickness versus printing (coating) speed relationship of the blend films printed at (a) 25 and 105 $^{\circ}$ C coating temperatures while maintaining the same blade angle of 7° ; (b) 7 and 45 $^{\circ}$ at the same coating temperature of 105 $^{\circ}$ C; (c) uniformity comparison between films printed in the evaporation regime (1 mm/s) and LL regime (5 mm/s) at 105 $^{\circ}$ C and a blade angle of 45 $^{\circ}$.

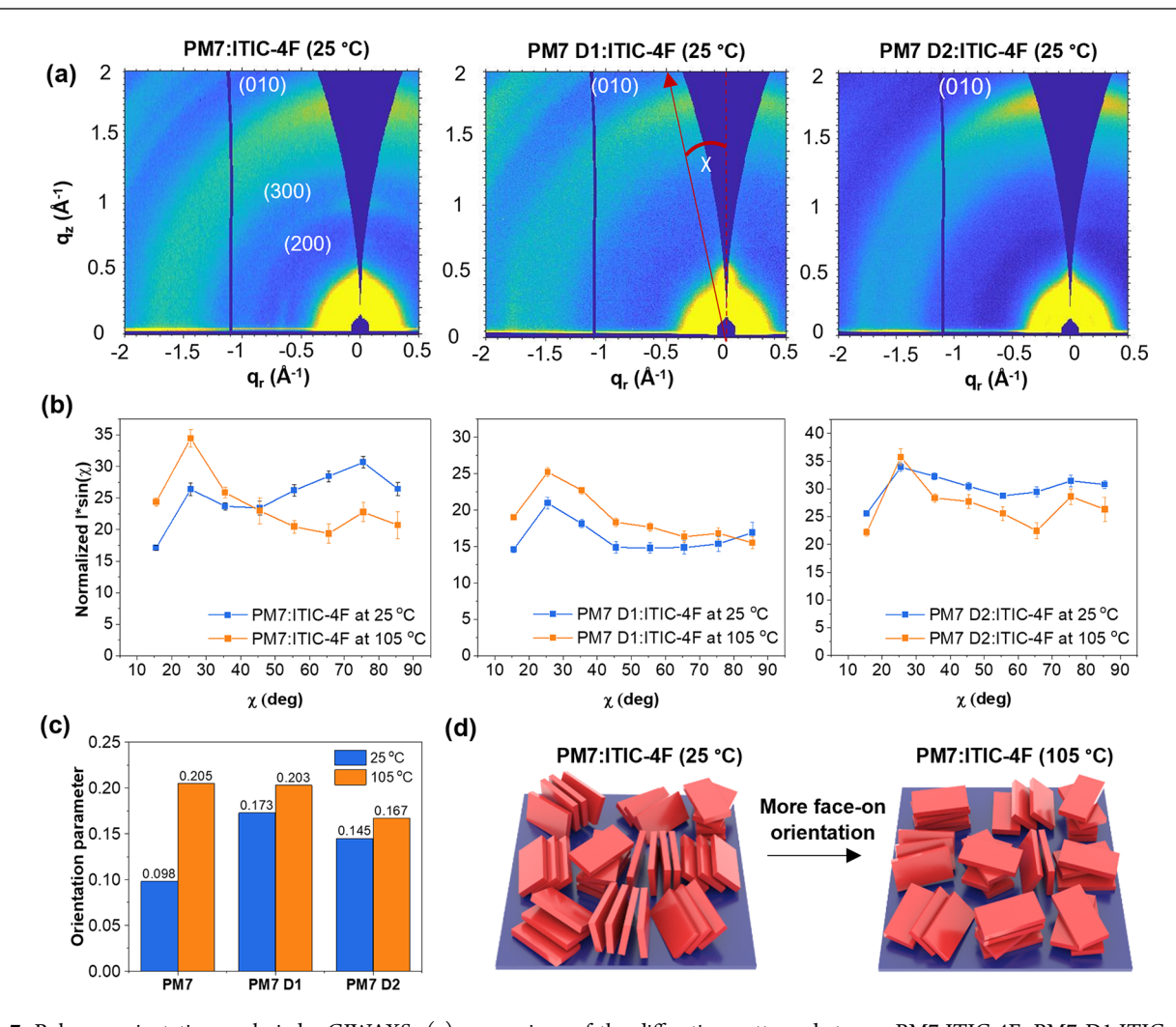


Figure 7. Polymer orientation analysis by GIWAXS: (a) comparison of the diffraction patterns between PM7:ITIC-4F, PM7 D1:ITIC-4F, and PM7 D2:ITIC-4F films printed at 25 °C temperature and 5 mm/s coating speed; (b) comparison of geometrically corrected orientation profiles using the π - π stacking peaks of the three blend films printed at 25 and 105 °C, respectively. In these plots, χ = 0° represents face-on orientation and χ = 90° represents edge-on orientation; (c) Herman's orientation parameter value comparison for three blend films printed at 25 and 105 °C to quantify the orientation change with respect to temperature; (d) illustration of molecular orientation change for the PM7:ITIC-4F blend film with respect to the coating substrate temperature.

temperatures to investigate the effect of substrate temperature on the solid-state morphology and device performance of OSCs. Therefore, we first determined how each of the processing parameters affect the film thickness and uniformity. To demonstrate how the film thickness and uniformity are affected by the processing parameters, we take PM7:ITIC-4F

film deposition as an example to show thickness as a function of coating speed relationship by (1) varying the substrate temperatures while keeping the blade angle constant (Figure 6a) and (2) varying the blade angles while keeping the substrate temperature constant (Figure 6b). As shown in Figure 6a, when the substrate temperature is 25 °C with a

blade angle of 7°, the film thickness decreases as the coating speed increases from 0.01 to ≈0.5 mm/s. This inverse relationship between the coating speed and film thickness corresponds to the evaporation regime⁵³ where the solution evaporation rate governs the relationship between the final film thickness and the coating speed. In this regime, we observe poor film uniformity (Figure 6c) due to stick-and-slip meniscus instability caused by a competition between pinning and depinning forces at the contact line. 54,55 On the other hand, in the Landau-Levich (LL) regime where the film thickness increases with coating speed, the deposited films are more uniform, which is desirable to reduce device-to-device performance variations (Figure 6c). Although the films are more uniform in the LL regime, the film thickness changes substantially when the substrate temperature is increased from 25 to 105 °C at a blade angle of 7° (the red plot in Figure 6a). In fact, we can see that the entire thickness versus coating speed relationship (both evaporation and LL regime) shifts to the right due to an increased evaporation rate and the change in the physical properties of the solution at an elevated temperature. Due to this shift, the film thickness is significantly reduced in the LL regime from ≈100 to ≈50 nm when increasing the substrate temperature from 25 to 105 °C while maintaining the same coating speed of 5 mm/s, as indicated by the dashed line in Figure 6a. To increase the film thickness without changing the concentration of the solution or the coating speed at a substrate temperature of 105 °C, we increased the blade angle from 7 to 45° , which shifted the entire curve upward as shown in Figure 6b resulting in the final thickness of ≈100 nm at 5 mm/s, as indicated by the dashed line. We attribute this upward shift to the increase in the back meniscus height, allowing us to vary the film thickness at any substrate temperature without changing the solution concentration or the coating speed.

Blend Film Morphology and Device Performance **Characterization.** Using the abovementioned approach to deposit thin uniforms films, we firstly investigated the solidstate morphology of the blend films blade coated at low (25 °C) and high (105 °C) substrate temperatures using GIWAXS. In Figure 7a, we show the 2D GIWAXS images of the blend films printed at 25 °C where all blend films exhibit in- and outof-plane (010) peaks at around $q \approx 1.8 \text{ Å}^{-1}$, which correspond to edge-on and face-on π - π stacking, respectively, with respect to the substrate. We attribute the $\pi-\pi$ stacking peaks to the polymer backbone stacking because all neat polymer films possess a (010) peak while the neat acceptor film has an amorphous halo, which does not contribute to the observed $\pi - \pi$ stacking peak of the blend film (Figure S15). Furthermore, all blend films exhibit lamellar stacking peaks (100) around $q \approx 0.3 \text{ Å}^{-1}$, as shown in Figure S16, which represents the color scale-adjusted GIWAXS patterns and the linecut profiles. The peak locations and FWHM of (010) and (100) peaks are summarized in Table S4. Based on the location of the (100) and (010) peaks, lamellar and π - π stacking distances for PM7:ITIC-4F, PM7 D1:ITIC-4F, and PM7 D2:ITIC-4F blend films processed at room temperature were obtained, as shown in Table 2. Although PM7:ITIC-4F has the shortest lamellar stacking distance, its $\pi - \pi$ stacking distance is larger (3.53 Å) than those of PM7 D1 and D2 blend films (3.42 and 3.45 Å). Interestingly, when a high substrate temperature (105 °C) is used for blade coating (2D GIWAXS patterns and the linecut profiles of these films are shown in Figure S17), the π - π stacking distance for PM7:ITIC-4F

Table 2. Lamellar and π - π Stacking Distances Obtained from GIWAXS

| samples | lamellar stacking distance (Å) | π - π stacking distance (Å) |
|-------------------------|-----------------------------------|-------------------------------------|
| PM7:ITIC-4F (25 °C) | 19.7 | 3.53 |
| PM7:ITIC-4F (105 °C) | 19.6 | 3.44 |
| PM7 D1:ITIC-4F (25 °C) | 22.4 | 3.42 |
| PM7 D1:ITIC-4F (105 °C) | 22.8 | 3.42 |
| PM7 D2:ITIC-4F (25 °C) | 21.6 | 3.45 |
| PM7 D2:ITIC-4F (105 °C) | 21.9 | 3.44 |

decreases from 3.53 to 3.44 Å whereas those of PM7 D1:ITIC-4F and PM7 D2:ITIC-4F remain almost unchanged (Table 2). We note that this result is highly consistent with the temperature-dependent fibrillar aggregates of PM7 and temperature-resilient properties of PM7 D1 and D2 in the solution state. In particular, since the fibrillar aggregates in the solution state already exhibit a large $\pi-\pi$ stacking distance of 3.65 Å, these aggregates may be directly translated to the blend films, thereby resulting in the large $\pi-\pi$ stacking distance observed in the room-temperature processed films.

We further compare the polymer orientation distribution of the three polymer blend films using the molecular orientation analysis, as described in earlier works. 56-58 The pole figures shown in Figure 7b are obtained by plotting the intensity of the (010) peak as a function of the azimuthal angle, χ , with 10° interval starting from 0 to 90° that represents face-on and edge-on crystallites, respectively. The (010) peak intensity at each angle is obtained by peak deconvolution due to the overlap of the amorphous and $\pi - \pi$ stacking peaks, as previously reported.⁵⁶ The obtained peak intensities are then normalized by their exposure time and irradiated volume and multiplied with sinx, which corrects the intensity underestimation at high χ due to the scattering geometry. Based on the analysis, we observe that the molecular orientation of the PM7:ITIC-4F blend film leads to a measurable change with respect to the coating temperature, as shown in Figure 7b in which the polymer orientation switches from a more isotropic population to a population with predominantly face-on orientation, as illustrated in Figure 7d. On the other hand, in the PM7 D1 and D2 blend films, we observe only a slight enhancement of the face-on population (Figure 7b). The extent of molecular orientation change can be more clearly quantified by calculating the Herman's orientation parameter $(S)^{59,60}$ from the (010) π – π stacking peak. The S parameter ranges from a value of -0.5, which corresponds to a complete edge-on population, to a value of 1, which is a total face-on population when the director is chosen as the surface normal. The S value of 0 corresponds to a mixture of both face-on and edge-on orientations. Based on Figure 7c, the PM7 blend film printed at 25 °C shows a value of 0.098, which represents an isotropic population whereas the PM7 D1 and D2 blend films printed at 25 °C are more face-on with S values of 0.173 and 0.145, respectively. At a high coating temperature of 105 °C, there is an increase in the S value for PM7 reaching 0.205 while only a slight improvement is observed for PM7 D1 and D2, indicating that their molecular orientation in the solid state is less dependent on the substrate temperature as compared to PM7. We attribute this isotropic orientation of the PM7 blend film printed at 25 °C to the fibrillar aggregates observed in solution, which may already possess their thermodynamically favorable orientations in the solution state.

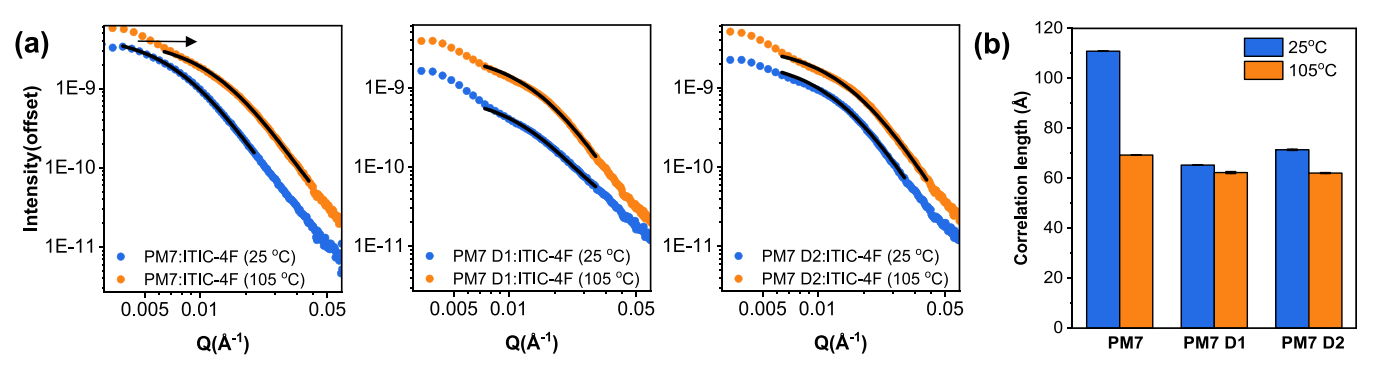


Figure 8. Blend film morphology characterization using RSoXS measurements. (a) Intensity versus q plots of all three polymer blend films printed at 25 and 105 $^{\circ}$ C temperatures where the arrows represent scattering due to surface roughness of SiN. (b) Correlation length comparison of the blend films obtained from the DAB model with a flat background.

To investigate the phase-separated structures of the blend films, we use resonant soft X-ray scattering (RSoXS)⁶¹ whereby the X-ray energy can be tuned to the aromatic C 1s $\rightarrow \pi^*$ to improve the contrast between the donor and acceptor domains. Although RSoXS of OSC systems are often applied at a single energy that delivers high scattering contrast, the origin of that contrast cannot be determined from a single energy. Possible origins of contrasts include compositional contrast between two or more OSC components and compositional contrast between those components and vacuum (roughness at the top interface) or SiN (roughness at the bottom interface). Orientational contrast is also possible wherein the contrast comes from between differently oriented populations of a single component or between non-isotropic populations of multiple components. Orientational fluctuations in a compositionally homogeneous film can give rise to considerable scattering intensity and features describing the length scales of orientational heterogeneity.⁶² The key to unraveling the origins of contrast in an RSoXS measurement is the detailed energy dependence of the total scattering intensity/invariant (TSI), the expectation of which for binary pairs of materials has been shown to be directly calculable from measured spectroscopic dielectric functions by Ferron et al. 63 As our data was collected only at 90° incidence, we will compare a quasi-TSI to calculated binary contrast functions under the assumption that the scattering intensity varies along the unmeasured thickness axis the same way as along the lateral axes.

We begin with RSoXS data obtained at 284.8 eV for which the scattering intensity reaches maximum (Figure 8a), with other energies shown in Figure S18. The PM7:ITIC-4F blend film exhibits a shift in the shoulder peak location to higher Q at the higher processing temperature as indicated by the arrow, indicating a decrease in characteristic length scale, whereas the shoulder peaks from PM7 D1 and PM7 D2 blend films do not shift as significantly with increasing processing temperatures. For PM7 D1 and D2 blend films, an additional shoulder peak at low Q (\approx 0.005 Å⁻¹), also seen in the Kratky plots (Figure S19), was found to be attributable to our SiN substrate as it is observed from RSoXS patterns of the blank substrate (Figure S20). The detailed energy dependence of the scattering intensity provides further confidence that this peak originates from roughness at the SiN-polymer interface; an integrated scattering intensity of this peak near $\approx 0.005 \text{ Å}^{-1}$ compares well to binary contrast functions between SiN and the hydrocarbons, as calculated by the method described in Ferron et al. (Figure S21a, b), whereas an integrated scattering intensity of the higher-Q peak does not appear to be influenced by SiN roughness (Figure S21a,c). It is also possible to rule out a top interface roughness contribution by examining vacuum contrast functions of all neat materials and their material contrast functions (donor and acceptor), as presented in Figure S22a. Our experimentally obtained TSI versus energy plots (Figure S22b) do not resemble these vacuum contrast functions. This result is consistent with film topology; all blend film samples exhibit rather smooth surfaces with root mean square (RMS) value of less than 5 nm as shown in Figure S23, where PM7 D1 and D2 exhibit even less than 1 nm.

We can thus narrow down the possible origins of RSoXS contrast of the principal scattering features to material and/or orientation contrasts. To develop anisotropic dielectric functions, we obtained incident-angle-dependent near edge X-ray absorption fine structure (NEXAFS) spectroscopy of the neat materials (Figure S24). These NEXAFS spectra were converted into real and imaginary indexes of refraction contributions δ and β , respectively, using a Kramers-Kronig transform.⁶⁴ Contrast between ordinary and extraordinary orientations of each component and the combinatorial distributions between the two components were then calculated (Figure S25). Pure compositional contrast between OSC components would be represented only by the contrast between isotropic, or NEXAFS "magic angle" components. We observe that the TSI vs energy plots do not exactly match the magic angle binary contrast function, suggesting that orientational effects cannot be neglected (Figure S25). This conclusion is consistent with the significant pattern anisotropy that is observed in our raw patterns (Figure S26). No single binary contrast function exactly matches our measured TSI vs energy, which suggests that a distribution of orientations of one or both components is responsible for the contrast.

Although we find that the scattering features are the result of a mixture of orientational and compositional heterogeneity, the center-to-center distance or spacing of regions with homologous orientation and/or composition is still relevant to the blend morphology and charge transport landscape of OSCs. Therefore, using the Debye—Anderson—Brumberger (DAB) model derived for a randomly distributed two-phase system from autocorrelation function, 65 we obtained the correlation length corresponding to the average distance between two phases, as shown in Figure 8b (values are summarized in Table 3). We note that scattering anisotropy does not influence the DAB model fitting significantly in the parallel and perpendicular directions with respect to the electric field (Figure S27 and Table S5), suggesting that the shape of the domains has

Table 3. Correlation Length Obtained from the DAB Model

| samples | correlation length (Å) ^a | | |
|-------------------------|-------------------------------------|--|--|
| PM7:ITIC-4F (25 °C) | 110.9 ± 0.1 | | |
| PM7:ITIC-4F (105 °C) | 69.3 ± 0.1 | | |
| PM7 D1:ITIC-4F (25 °C) | 65.3 ± 0.1 | | |
| PM7 D1:ITIC-4F (105 °C) | 62.3 ± 0.4 | | |
| PM7 D2-ITIC-4F (25 °C) | 71.4 ± 0.3 | | |
| PM7 D2:ITIC-4F (105 °C) | 62.1 ± 0.2 | | |

^aThe uncertainties here represent the model fitting error.

minimal influence on the scattering features although it is nonnegligible. Nevertheless, since the domain form factor and structure factor cannot be uniquely separated, we obtained a single length scale using the DAB model based on the circularly averaged scattering profiles. Based on Figure 8b and Table 3, the PM7:ITIC-4F blend film processed at room temperature exhibits the largest correlation length, which substantially decreases when the film is processed at high temperatures. This result is consistent with the order-disorder transition of fiber aggregates of PM7, leading to the processing temperature-sensitive morphology. In contrast, PM7 D1 and D2 yield a smaller correlation length, which is almost unaffected by the processing temperature, suggesting that the temperature-resilient amorphous polymer network aggregates help to maintain the phase separated structures of the blend film.

To correlate the solution aggregate structures and the blend film morphology to the device performance of OSCs, we carried out device fabrication using substrate temperatures of 25, 65, and 105 $^{\circ}$ C from a room-temperature solution (using

both hot solution (105 °C) and room-temperature solution (25 °C) leads to similar performances as shown in Figure S28 and Table S6 due to the small amount of solution ($\approx 5 \mu L$) used for blade coating). At each coating temperature, we retained the coating speed at 5 mm/s and varied the blade angle, as discussed previously to achieve uniform films with optimal thickness of ≈ 80 nm. The I-V performance of inverted geometry devices with an ITO/ZnO/active layer/ MoO₃/Ag architecture in which ITO acts as an electron collecting electrode (cathode) and Ag as the hole collecting electrode (anode) is shown in Figure 9a-c. In Figure 9d, we observe that the PM7:ITIC-4F device performance changes substantially with increasing coating temperature, showing an ≈50% increase in the PCE from 5.8 to 8.7% when PM7 converted from fiber aggregates to network aggregates in solution upon heating. In comparison, the PCEs of the PM7 D1- and D2-based devices exhibited less statistical variation with only about ≈10 and ≈15% increases with increasing temperature, respectively. The drastic device performance change in the PM7-based devices with increasing coating temperature is mainly attributed to the short-circuit current (J_{SC}) and fill factor (FF) improvement (Table 4, Figure 9e,f), which are highly correlated with the morphology of the blend films. On the other hand, we do not observe any trend in $V_{\rm OC}$ values Figure 9g, which could be due to factors unrelated to morphology change such as defects during device fabrication (e.g., thermal evaporation at high temperatures), which are inconsistent from sample to sample. At low coating temperature, the PM7 blend film morphology exhibits large domains where polymers are oriented isotropic while PM7 D1 and D2 form small domains where polymers are oriented predom-

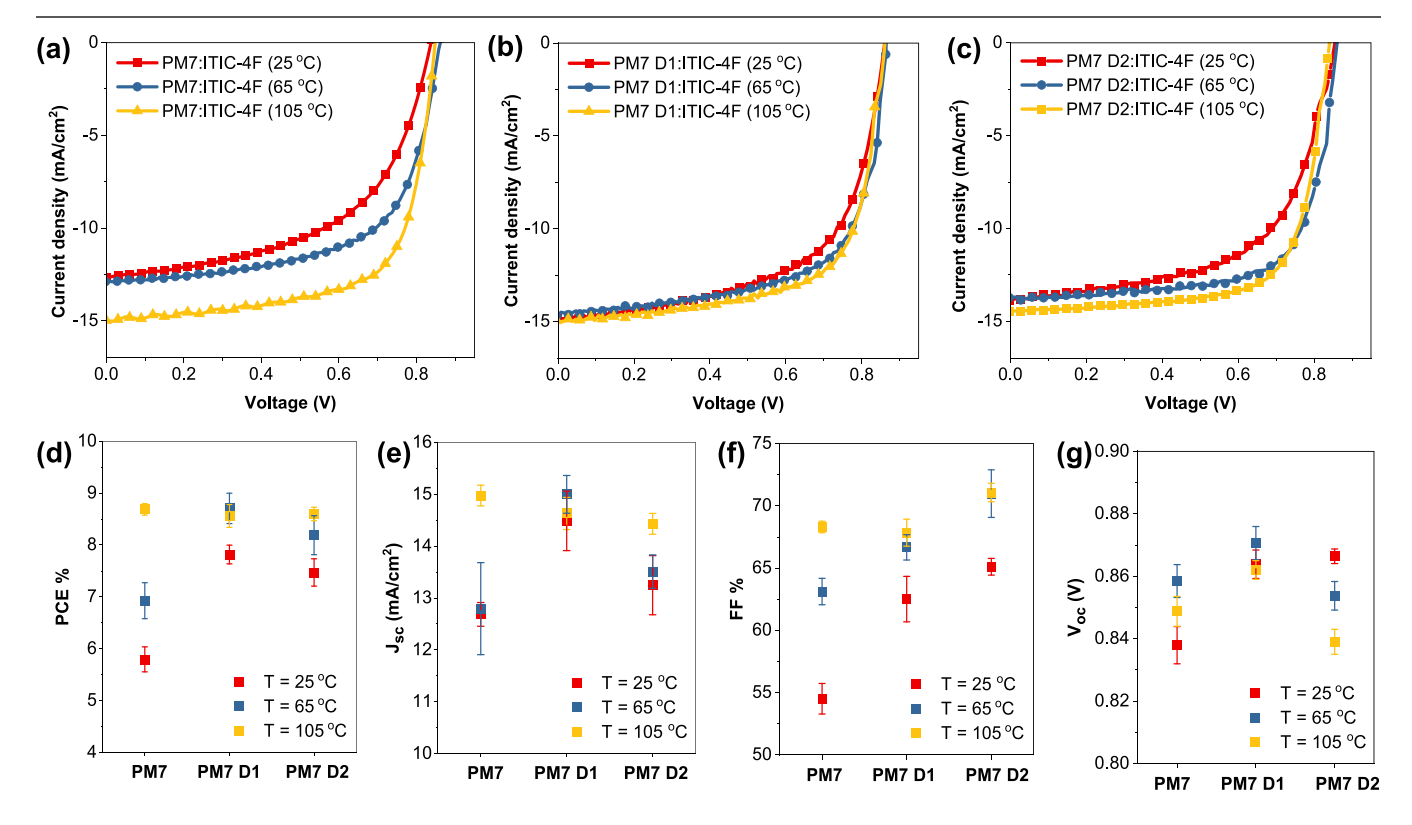


Figure 9. Device characterization results: current–voltage (J–V) curves of (a) PM7:ITIC-4F, (b) PM7 D1:ITIC-4F, and (c) PM7 D2:ITIC-4F devices fabricated at three different processing temperatures. Comparison of device performances: (d) PCE, (e) J_{SC} (f) FF, and (g) V_{OC} in which the average and error (sample standard deviation) are based on ≈10–15 devices. The solution concentration is 20 mg/mL for the polymer and acceptor, and the coating speed is maintained at 5 mm/s at all conditions. The blade angle is varied to optimize the thickness for all films ≈80 nm.

Table 4. Device Performance Results of the Blend Films Printed at Varying Temperatures

| samples | PCE (%) | FF (%) | J_{SC} (mA/cm ²) | $V_{\rm OC}$ (V) |
|-------------------------|---------------|--------------|--------------------------------|------------------|
| PM7:ITIC-4F (25 °C) | 5.8 ± 0.2 | 55 ± 1.3 | 12.7 ± 0.2 | 0.84 ± 0.01 |
| PM7:ITIC-4F (65 °C) | 6.9 ± 0.4 | 63 ± 1.0 | 12.8 ± 0.9 | 0.86 ± 0.01 |
| PM7:ITIC-4F (105 °C) | 8.7 ± 0.1 | 68 ± 0.5 | 15.0 ± 0.2 | 0.85 ± 0.01 |
| PM7 D1:ITIC-4F (25 °C) | 7.8 ± 0.2 | 62 ± 1.8 | 14.5 ± 0.6 | 0.86 ± 0.01 |
| PM7 D1:ITIC-4F (65 °C) | 8.7 ± 0.3 | 67 ± 1.0 | 15.0 ± 0.4 | 0.87 ± 0.01 |
| PM7 D1:ITIC-4F (105 °C) | 8.6 ± 0.2 | 68 ± 1.1 | 14.6 ± 0.3 | 0.86 ± 0.01 |
| PM7 D2:ITIC-4F (25 °C) | 7.5 ± 0.3 | 65 ± 0.7 | 13.2 ± 0.6 | 0.87 ± 0.01 |
| PM7 D2:ITIC-4F (65 °C) | 8.2 ± 0.4 | 71 ± 1.9 | 13.5 ± 0.3 | 0.85 ± 0.01 |
| PM7 D2:ITIC-4F (105 °C) | 8.6 ± 0.1 | 71 ± 0.7 | 14.4 ± 0.2 | 0.84 ± 0.01 |

inantly face-on. This morphology difference correlates well with the inferior $J_{\rm SC}$ and FF of the PM7 polymer-based devices fabricated at low coating temperature as the charge generation and transport are reduced due to the large domains and the unfavorable molecular orientation. When the coating temperature is increased, we observe a significant change in the device performance of PM7, which also corresponds to the morphology change observed in the solid state, more specifically the domain size reduction, closer $\pi-\pi$ stacking, and enhancement of the face-on molecular orientation. For PM7 D1- and D2-based devices, the device performance resiliency is also correlated with their robust solid-state morphology, which is less sensitive to the processing temperature.

Overall, our film morphology and device performance results indicate that the initial solution-state aggregate structures of donor polymers largely determine the final film morphology and device performance of OSCs. We found that the large fiber-like aggregates formed in the solution state led to large $\pi-\pi$ stacking distance and large domain spacing without preferential molecular orientation while network-like aggregates resulted in shorter $\pi-\pi$ stacking and smaller domain spacing with predominantly face-on orientation. Since the small-molecule acceptor, ITIC-4F, is amorphous based on our GIWAXS results (Figure S15), we predict that the donor polymer aggregation in solution likely templates the film morphology, which has been demonstrated in other studies. 16,66,67

CONCLUSIONS

Previous studies have shown the importance of donor polymer solution-state aggregation on the morphology and device performance of OSCs. However, little is known about the exact structure of polymer aggregates in the solution state and how it determines the BHJ morphology and performance of OSCs. In this article, we have investigated the donor polymer aggregate structures of the PM7 polymer and its ester-functionalized derivatives with reduced backbone planarity, PM7 D1 and D2, to highlight the importance of polymer aggregate structures on the morphology, device performance, and processing temperature resiliency of blade-coated OSCs. By employing SAXS and microscopy measurements, we revealed that PM7 forms semi-crystalline fiber aggregates, whereas PM7 D1 and D2 lead to amorphous network-like aggregates of single polymer chains at

room temperature. Our DFT studies indicated that PM7 D1 and D2 polymers are more non-planar and flexible than PM7 due to their rotationally flexible ester-functionalized terthiophene acceptor moieties, which reduce the likelihood of forming large fiber-like aggregates observed in PM7. Furthermore, we demonstrated that these fiber aggregates yield OSCs with inferior device performance by leading to large $\pi - \pi$ stacking distance and large domain spacing without preferential molecular orientation in the blend film. We also observed that the fiber aggregates undergo a drastic orderdisorder transition with increasing solution temperature, yielding devices that are strongly dependent on the processing temperature. On the other hand, the amorphous network-like aggregates of PM7 D1 and D2 polymers not only showed an improved processing temperature resiliency but also yielded higher PCEs due to their favorable BHJ morphology consisting of short $\pi - \pi$ stacking distance, small domain spacing, and faceon dominant molecular orientation. Consistently, we found that PM7 yields improved performance when it formed amorphous network-like aggregates at high solution temperatures. Overall, our findings suggest that the polymer aggregate structure in the solution state determines the solid-state morphology, device performance, and processing resiliency of non-fullerene OSCs. In particular, we show that as compared to semi-crystalline fiber-like aggregates, forming amorphous network-like aggregates in the solution state improves the device performance and processing resiliency in blade-coated OSCs. Besides the two types of aggregate structures described in this work, polymer solutions can form other types of aggregates, which may impact the BHJ morphology and device properties. Therefore, further investigation will be needed to understand the impact of various types of polymer aggregates on the optoelectronic properties of OSCs.

■ EXPERIMENTAL SECTION

Material and Solution Preparation. The donor polymers (PM7, PM7 D1, and PM7 D2) used in this study were synthesized according to Jones et al.²³ with similar number average molecular weights between 38 and 41 kg/mol with dispersity below 2.5, as shown in Table S1. The molecular acceptor, ITIC-4F, with >99% purity was purchased from Brilliant Matters, Inc.* The neat polymer solutions were prepared by dissolving each polymer in chlorobenzene (anhydrous, 99.8%, Sigma-Aldrich, Inc.) to obtain a solution of 20 mg/mL concentration and stirred at 40 °C for over 12 h and cooled down to room temperature for 2-3 h before each experiment. The blend solutions for device fabrication were prepared by mixing each polymer with the small-molecule acceptor at a 1:1 weight ratio and dissolving the mixture in chlorobenzene to obtain a solution with a total concentration of 40 mg/mL. These blend solutions were also stirred at 40 °C for over 12 h and cooled to room temperature for 2-3 h before device fabrication.

*Certain commercial equipment, instruments, or materials are identified in this paper to foster understanding. Such identification does not imply recommendation or endorsement by the National Institute of Standards and Technology, nor does it imply that the materials or equipment identified are necessarily the best available for the purpose.

Density Functional Theory Calculations. DFT calculations were used for molecular geometry optimization and obtaining potential energy scans of the dihedral angles. All calculations were performed with the Gaussian 16 package by using the wB97xD method at the 6-31G (d, p) basis set. In all calculations, the long alkyl sidechains on both donor and acceptor moieties were replaced with methyl groups for simplification. To obtain the potential energy scans of a dihedral angle, molecular fragments relevant to the dihedral angle of interest were firstly optimized at the wB97xD/6-31G (d, p) level of

theory. These molecular fragments are provided in each potential energy scan plots. Afterward, a rigid scan where the single point energy of the optimized molecule was computed when the dihedral angle was varied from 0 to 180° at the 10° interval while fixing other dihedral angles. The resulting single-point energies were then plotted against the respective dihedral angle to obtain potential energy plots.

Solution-State Characterization. *UV–Vis Spectroscopy.* UV–vis (Cary 60 UV–Vis, Agilent) spectroscopy was used to measure the absorbance of 20 mg/mL polymer solutions in a short path length of 10 μ m quartz cell (Starna Cells). Before each solution measurement, a blank solvent measurement was taken for background subtraction. For temperature-dependent UV–vis measurements, a resistive heater and a thermocouple were incorporated into a metal sample holder to heat the solution to the desired temperature at a rate of 2–3 °C/min. Due to the low amount of solution in a narrow quartz cell, the highest temperature for UV–vis measurement in chlorobenzene solution was 75–85 °C before solution evaporation.

SAXS Experiments. SAXS experiments were performed at the 12-ID-B beamline of the Advanced Photon Resource at Argonne National Laboratory using a beamline energy of 13.3 keV at detector distances of 2 and 4 m to probe different scattering vector, Q, ranges. Before performing the polymer solution scattering measurements, the pure solvent background measurement was taken at each experimental temperature to ensure proper background subtraction. Both background and solution measurements were performed using flow cells, which were prepared by using a 1 mm-diameter quartz capillary connected to PTFE tubing by PTFE heat shrink tubing. Each polymer solution in the flow cell was cycled back and forth to avoid beam damage. Each solution measurement was taken at 0.1 s exposure time with an interval of 2-3 s for a total exposure time of 1 s. The obtained raw 2D scattering pattern was reduced to a 1D profile of intensity as a function of the scattering vector from which the solvent background was subtracted to obtain the scattering profile from the polymer only. The resulting scattering profiles were then fit to the model from ref 30 using the SasView program. For modeling fitting in SasView, we selected dI data for weighting, Levenberg-Marquardt with 200 steps for the algorithm where the uncertainties are determined from the covariance matrix, and χ^2 values and the residuals plot were used as the goodness of fit metrics.

Freeze-Drying Method for Imaging the Solution-State Aggregates. Freeze-drying experiments were conducted to image the structure of aggregates in solution by using microscopic techniques including AFM, scanning electron microscopy (SEM), and TEM. The freeze-drying process involves rapid freezing of polymer solutions in liquid ethane and propane mixture (63% propane and 37% ethane) followed by liquid nitrogen storage. The purpose of using the liquid ethane mixture is to ensure rapid freezing of the solution due to its large heat capacity and prevent polymer aggregation during the cooling process. The resulting frozen polymer solution is then quickly transferred to a Linkam stage at −120 °C under vacuum. The Linkam stage temperature is then slowly increased at a rate of 0.5 °C/min to -80 °C (far below the melting point of chlorobenzene solvent mp = -45 °C) followed by 6-8 h of constant monitoring with crosspolarized microscopy to ensure sublimation of all solvent. The sample is then imaged using AFM (Asylum Research Cypher) with tapping mode, and TEM (Hitachi H-9500). TEM-based electron diffraction measurements were also conducted to determine $\pi - \pi$ stacking in the freeze-dried samples. Electron diffraction was taken by a Gatan US1000 CCD camera equipped on a 300 kV Hitachi H9500 environmental TEM with a guarded ring LaB₆ cathode. Filament current was set automatically at 3.5 μ A to reduce beam damage during operation. Patterns were taken at 3 s exposure time each, and six images were summed to produce the final image. Beam block and astigmatism were removed and monitored upon azimuthal integration for the intensity line profile. The length scale was calibrated with an Au nanoparticle sample, and 4.08 Å was used as its lattice constant.

OSC Device Fabrication. OSCs were fabricated using the inverted architecture (glass/ITO/ZnO/polymer: ITIC:4F/MoO $_3$ /Ag). Before film deposition, 20 \times 15 cm ITO-patterned glass substrates (Ossila, Inc.) were cleaned by sonicating sequentially with

water, acetone, and finally isopropanol for 10 min each. The cleaned substrates were then dried with nitrogen and plasma treated (Harrick Plasma PDC-001-HP) for 6 min at 300 mT of dry air and high power (30 W). To deposit the electron transporting layer, ZnO solution was prepared by dissolving 1 g of zinc acetate dihydrate (Sigma-Aldrich) and 0.28 g of ethanolamine (Sigma-Aldrich) in 10 mL of 2methoxyethanol (Sigma-Aldrich) under vigorous stirring for over 12 h in air. This solution was then filtered with a 0.45 μ m PTFE syringe filter before deposition. The filtered solution was deposited on the cleaned ITO substrates by spin-coating for 30 s at 4000 rpm in an ambient atmosphere, which resulted in an active layer thickness of ≈20-30 nm measured by a Bruker Dektak XT profilometer. After spin-coating, the ZnO layer was annealed in air at 200 °C for 30 min followed by slow cooling to room temperature for active layer deposition. We find that it was important to anneal the substrates immediately after ZnO deposition to prevent device failures. The photoactive layer solution for all devices was prepared by dissolving the polymer and ITIC-4F (Sigma-Aldrich) at 1:1 (wt/wt) ratio in chlorobenzene without any additives. The resulting blend solution was stirred at 40 °C overnight and brought to room temperature 1–2 h before deposition. The photoactive layer was then blade coated on the ZnO-coated ITO-glass substrate at coating temperatures of 25, 65, and 105 °C at 5 mm/s coating speed. For blade coating, the substrates were firstly stabilized at the coating temperatures for about 5 min and the blade was kept at room temperature. To ensure the same film thickness when coating at different temperatures, the blade angle was varied from 10 to 55° with a solution volume of $\approx 5 \mu L$ (the wet width of the blade is around 6 mm). By varying the blade angle, the optimal film thickness for all devices was kept at \approx 80 nm. All thin films were then annealed in a nitrogen-filled glovebox at 100 °C for 10 min. Finally, 8 nm hole transporting layer and 120 nm of Ag electrode was deposited by using a Thermal Evaporator (Kurt J. Lesker Nano36) by slowly ramping the rate of deposition to 0.1 and 1 Å/s, respectively.

Device and Film Morphology Characterization. Device Characterization. The current density (J-V) curves were characterized by using an automated Solar Cell I-V Test System (Ossila) under AM 1.5G illumination (100 mW/cm) with a class AAA solar simulator (SciSun-150 by Sciencetech). Before each test, the solar simulator was calibrated by reference single-crystal Si cells (Sciencetech). Each sample includes eight pixels and a total of three samples, or 24 devices were tested under each condition for reliable experimental results. For calculating the device performance, the mismatch factor was not applied.

GIWAXS. GIWAXS measurements were performed at the 8-IDE beamline of the Advanced Photon Source at Argonne National Laboratory using an incident beam energy of 10.86 keV on a two-dimensional detector (PILATUS) with an incident angle of 0.14°. For sample preparation, ZnO was firstly deposited on a Si wafer followed by the photoactive layer deposition and thermal annealing the same way that all OSC devices were fabricated. From GIWAXS measurement, 2D scattering images were obtained and converted to 1D scattering profiles by using the beamline GIXSGUI package written for MATLAB. For molecular orientation analysis, the 1D GIWAXS pattern of intensity versus scattering vector was azimuthally integrated from $-10^{\circ} < \chi < -80^{\circ}$ with a 5° interval to yield an intensity versus the χ angle.

RSoXS. RSoXS data were collected at the Advanced Light Source beamline 11.0.1.2 in transmission geometry. For sample preparation, the photoactive layer was blade coated and thermally annealed using the same device fabrication conditions on a polystyrene sulfonate (PSS) film, which was spin coated from a 10% PSS solution in water. The PSS solution was stirred overnight at room temperature before depositing on a Si wafer substrate. After photoactive layer deposition, the sample on a Si substrate was immersed in water, which dissolved the PSS layer and separated the sample from the substrate. The sample was then picked up with a 1 \times 1 mm, 100 nm-thick Si $_3N_4$ membrane supported on a 5 \times 5 mm, 200 μ m-thick Si frame (Norcada) and transferred into the vacuum chamber for RSoXS measurement. RSoXS measurements were performed at the beam energy from 270 to 290 eV with 5 s of exposure time per scan. The

collected 2D scattering images were then converted into 1D profiles using the Nika package supported in the Igor Pro environment. The obtained 1D profiles were normalized by the incoming beam intensity, I_0 , provided by a gold mesh and photodiode, and total illuminated volume, which is determined by the multiplication of the illumination area and sample thickness. Since the total illuminated area is the same for all films, thickness measurements were used to normalize the intensity.

Angular NEXAFS TEY Measurements. To determine vacuum and binary contrast functions, we have obtained NEXAFS TEY measurements on the neat films. The samples for NEXAFS TEY were prepared by coating the neat films on a 1×1 cm Si wafer using the same conditions used for device fabrication. The samples were then measured at the beam energy from 270 to 320 eV using different polarization angles while fixing the incident angle. NEXAFS data were double normalized by the Au mesh current and photodiode calibration followed by pre-edge normalization using the QANT software package supported in Igor Pro environment.

Film Thickness Measurements. Film thickness was measured by using the Bruker Dektak XT profilometry with the stylus force of 3 mg with a scan range of $1000-2000~\mu m$. For thickness measurements, a part of the film was removed with a cotton swab with toluene solvent. The thickness measurements were repeated on three to five different positions to obtain the average and standard deviation.

ASSOCIATED CONTENT

Supporting Information

The Supporting Information is available free of charge at https://pubs.acs.org/doi/10.1021/acs.chemmater.2c02141.

Polymer synthesis results; supporting details for the solution-state characterization results; details of SAXS fitting; supporting information for the DFT calculation results; blend solution-state characterization results; supporting information for GIWAXS measurements; details of RSoXS analysis; device performance results for solution temperature variation (PDF)

AUTHOR INFORMATION

Corresponding Author

Ying Diao — Department of Chemical and Biomolecular Engineering, University of Illinois Urbana-Champaign, Urbana, Illinois 61801, United States; Department of Materials Science and Engineering, University of Illinois at Urbana-Champaign, Urbana, Illinois 61801, United States; Department of Chemistry, University of Illinois Urbana-Champaign, Urbana, Illinois 61801, United States; orcid.org/0000-0002-8984-0051; Email: yingdiao@illinois.edu

Authors

Azzaya Khasbaatar — Department of Chemical and Biomolecular Engineering, University of Illinois Urbana-Champaign, Urbana, Illinois 61801, United States; orcid.org/0000-0002-4145-3511

Andrew Cheng – Department of Chemical and Biomolecular Engineering, University of Illinois Urbana-Champaign, Urbana, Illinois 61801, United States

Austin L. Jones — School of Chemistry and Biochemistry, School of Materials Science and Engineering, Center for Organic Photonics and Electronics, Georgia Tech Polymer Network, Georgia Institute of Technology, Atlanta, Georgia 30332, United States; orcid.org/0000-0002-3035-6548

Justin J. Kwok – Department of Materials Science and Engineering, University of Illinois at Urbana-Champaign, Urbana, Illinois 61801, United States; orcid.org/0000-0003-3909-4369

Sang Kyu Park — Department of Chemical and Biomolecular Engineering, University of Illinois Urbana-Champaign, Urbana, Illinois 61801, United States

Jessica K. Komar – Department of Chemical and Biomolecular Engineering, University of Illinois Urbana-Champaign, Urbana, Illinois 61801, United States

Oliver Lin – Department of Chemistry, University of Illinois Urbana-Champaign, Urbana, Illinois 61801, United States

Nicholas E. Jackson – Department of Chemistry, University of Illinois Urbana-Champaign, Urbana, Illinois 61801, United States; orcid.org/0000-0002-1470-1903

Qian Chen — Department of Chemical and Biomolecular Engineering, University of Illinois Urbana-Champaign, Urbana, Illinois 61801, United States; Department of Materials Science and Engineering, University of Illinois at Urbana-Champaign, Urbana, Illinois 61801, United States; Department of Chemistry, University of Illinois Urbana-Champaign, Urbana, Illinois 61801, United States; orcid.org/0000-0002-1968-441X

Dean M. DeLongchamp — National Institute of Standards and Technology, Gaithersburg, Maryland 20899, United States; Occid.org/0000-0003-0840-0757

John R. Reynolds — School of Chemistry and Biochemistry, School of Materials Science and Engineering, Center for Organic Photonics and Electronics, Georgia Tech Polymer Network, Georgia Institute of Technology, Atlanta, Georgia 30332, United States; orcid.org/0000-0002-7417-4869

Complete contact information is available at: https://pubs.acs.org/10.1021/acs.chemmater.2c02141

Author Contributions

All authors have given approval to the final version of the manuscript.

Notes

The authors declare no competing financial interest.

ACKNOWLEDGMENTS

This work was primarily supported by the Office of Naval Research under grant numbers N00014-19-1-2146 (Y.D.), N00014-22-1-2202 (Y.D.), N00014-21-1-2087 (J.R.R), and N00014-22-1-2185 (J.R.R). A.K. acknowledges the Parr fellowship and 3 M Corporate fellowship. J.J.K. and Y.D. acknowledge support by the NSF CAREER award under Grant No. 18-47828. O.L. and Q.C. acknowledge support from Air Force Office of Scientific Research grant AFOSR FA9550-20-1-0257. This research used resources of the Advanced Photon Source, a U.S. Department of Energy (DOE) Office of Science User Facility, operated for the DOE Office of Science by Argonne National Laboratory under Contract No. DE-AC02-06CH11357 and the Advanced Light Source, a U.S. DOE Office of Science User Facility under contract no. DE-AC02-05CH11231. The research also used facilities of the Materials Research Laboratory Central Research Facilities, University of Illinois. Extraordinary facility operations were supported in part by the DOE Office of Science through the National Virtual Biotechnology Laboratory, a consortium of DOE national laboratories focused on the response to COVID-19, with funding provided by the Coronavirus CARES Act. The authors thank beamline scientists Joseph W. Strazalka of the Advanced Photon Source (Beamline 8-ID-E), Argonne Na-

tional Laboratory, Cheng Wang of the Advanced Light Source (Beamline 11.0.1.2), Eliot Gann of the National Institute of Standards and Technology, and Xiaobin Zuo for facilitating the GIWAXS, RSoXS, NEXAFS, and SAXS measurements, respectively. We are also grateful to the Diao group members Kyung Sun Park for training on freeze-drying experiments and providing helpful discussions on analyzing GIWAXS results and Jong-Hoon Lee for assistance in troubleshooting device measurements. The authors also appreciate Peter J. Dudenas and Bijal Patel from the National Institute of Standards and Technology for the helpful discussions related to RSoXS analysis.

REFERENCES

- (1) Li, G.; Shrotriya, V.; Huang, J.; Yao, Y.; Moriarty, T.; Emery, K.; Yang, Y. High-efficiency solution processable polymer photovoltaic cells by self-organization of polymer blends. *Nat. Mater.* **2005**, *4*, 864–868.
- (2) Davy, N. C.; Sezen-Edmonds, M.; Gao, J.; Lin, X.; Liu, A.; Yao, N.; Kahn, A.; Loo, Y.-L. Pairing of near-ultraviolet solar cells with electrochromic windows for smart management of the solar spectrum. *Nat. Energy* **2017**, *2*, 17104.
- (3) Pecunia, V.; Occhipinti, L. G.; Hoye, R. L. Z. Emerging Indoor Photovoltaic Technologies for Sustainable Internet of Things. *Adv. Energy Mater.* **2021**, *11*, 2100698.
- (4) Cui, Y.; Xu, Y.; Yao, H.; Bi, P.; Hong, L.; Zhang, J.; Zu, Y.; Zhang, T.; Qin, J.; Ren, J.; et al. Single-Junction Organic Photovoltaic Cell with 19% Efficiency. *Adv. Mater.* **2021**, *33*, 2102420.
- (5) Schneider, S. A.; Gu, K. L.; Yan, H.; Abdelsamie, M.; Bao, Z.; Toney, M. F. Controlling Polymer Morphology in Blade-Coated All-Polymer Solar Cells. *Chem. Mater.* **2021**, *33*, 5951–5961.
- (6) Krebs, F. C. Fabrication and processing of polymer solar cells: A review of printing and coating techniques. *Sol. Energy Mater. Sol. Cells* **2009**, 93, 394–412.
- (7) Zhao, K.; Hu, H.; Spada, E.; Jagadamma, L. K.; Yan, B.; Abdelsamie, M.; Yang, Y.; Yu, L.; Munir, R.; Li, R.; et al. Highly efficient polymer solar cells with printed photoactive layer: rational process transfer from spin-coating. *J. Mater. Chem. A* **2016**, *4*, 16036–16046.
- (8) Dong, S.; Zhang, K.; Jia, T.; Zhong, W.; Wang, X.; Huang, F.; Cao, Y. Suppressing the excessive aggregation of nonfullerene acceptor in blade-coated active layer by using n-type polymer additive to achieve large-area printed organic solar cells with efficiency over 15%. *EcoMat* **2019**, *1*, No. e12006.
- (9) Zhao, W.; Zhang, S.; Zhang, Y.; Li, S.; Liu, X.; He, C.; Zheng, Z.; Hou, J. Environmentally Friendly Solvent-Processed Organic Solar Cells that are Highly Efficient and Adaptable for the Blade-Coating Method. *Adv. Mater.* **2018**, *30*, 1704837.
- (10) Ro, H. W.; Downing, J. M.; Engmann, S.; Herzing, A. A.; DeLongchamp, D. M.; Richter, L. J.; Mukherjee, S.; Ade, H.; Abdelsamie, M.; Jagadamma, L. K.; et al. Morphology changes upon scaling a high-efficiency, solution-processed solar cell. *Energy Environ. Sci.* **2016**, *9*, 2835–2846.
- (11) Zhao, H.; Naveed, H. B.; Lin, B.; Zhou, X.; Yuan, J.; Zhou, K.; Wu, H.; Guo, R.; Scheel, M. A.; Chumakov, A.; et al. Hot Hydrocarbon-Solvent Slot-Die Coating Enables High-Efficiency Organic Solar Cells with Temperature-Dependent Aggregation Behavior. *Adv. Mater.* 2020, 32, 2002302.
- (12) Ma, W.; Yang, G.; Jiang, K.; Carpenter, J. H.; Wu, Y.; Meng, X.; McAfee, T.; Zhao, J.; Zhu, C.; Wang, C.; Ade, H.; Yan, H. Influence of Processing Parameters and Molecular Weight on the Morphology and Properties of High-Performance PffBT4T-2OD: PC71BM Organic Solar Cells. Adv. Energy Mater. 2015, 5, 1501400.
- (13) Constantinou, I.; Lai, T.-H.; Zhao, D.; Klump, E. D.; Deininger, J. J.; Lo, C. K.; Reynolds, J. R.; So, F. High Efficiency Air-Processed Dithienogermole-Based Polymer Solar Cells. *ACS Appl. Mater. Interfaces* **2015**, *7*, 4826–4832.

- (14) Hernandez, J. L.; Deb, N.; Wolfe, R. M. W.; Lo, C. K.; Engmann, S.; Richter, L. J.; Reynolds, J. R. Simple transfer from spin coating to blade coating through processing aggregated solutions. *J. Mater. Chem. A* **2017**, *5*, 20687–20695.
- (15) Wu, Y.; Schneider, S.; Walter, C.; Chowdhury, A. H.; Bahrami, B.; Wu, H.-C.; Qiao, Q.; Toney, M. F.; Bao, Z. Fine-Tuning Semiconducting Polymer Self-Aggregation and Crystallinity Enables Optimal Morphology and High-Performance Printed All-Polymer Solar Cells. J. Am. Chem. Soc. 2020, 142, 392–406.
- (16) Qian, D.; Ye, L.; Zhang, M.; Liang, Y.; Li, L.; Huang, Y.; Guo, X.; Zhang, S.; Tan, Z.; Hou, J. Design, Application, and Morphology Study of a New Photovoltaic Polymer with Strong Aggregation in Solution State. *Macromolecules* **2012**, *45*, 9611–9617.
- (17) Liu, Y.; Zhao, J.; Li, Z.; Mu, C.; Ma, W.; Hu, H.; Jiang, K.; Lin, H.; Ade, H.; Yan, H. Aggregation and morphology control enables multiple cases of high-efficiency polymer solar cells. *Nat. Commun.* **2014**, *5*, 5293.
- (18) Pelse, I.; Jones, A. L.; Richter, L. J.; Reynolds, J. R. Probing Crystallization Effects when Processing Bulk-Heterojunction Active Layers: Comparing Fullerene and Nonfullerene Acceptors. *Chem. Mater.* **2021**, 33, 657–667.
- (19) Guo, C.; Li, D.; Wang, L.; Du, B.; Liu, Z.-X.; Shen, Z.; Wang, P.; Zhang, X.; Cai, J.; Cheng, S.; et al. Cold-Aging and Solvent Vapor Mediated Aggregation Control toward 18% Efficiency Binary Organic Solar Cells. *Adv. Energy Mater.* **2021**, *11*, 2102000.
- (20) Seo, S.; Kim, J.; Kang, H.; Lee, J.-W.; Lee, S.; Kim, G.-U.; Kim, B. J. Polymer Donors with Temperature-Insensitive, Strong Aggregation Properties Enabling Additive-Free, Processing Temperature-Tolerant High-Performance All-Polymer Solar Cells. *Macromolecules* **2021**, *54*, 53–63.
- (21) Chen, H.-Y.; Hou, J.; Zhang, S.; Liang, Y.; Yang, G.; Yang, Y.; Yu, L.; Wu, Y.; Li, G. Polymer solar cells with enhanced open-circuit voltage and efficiency. *Nat. Photonics* **2009**, *3*, 649–653.
- (22) Zhang, M.; Guo, X.; Ma, W.; Ade, H.; Hou, J. A Polythiophene Derivative with Superior Properties for Practical Application in Polymer Solar Cells. *Adv. Mater.* **2014**, *26*, 5880–5885.
- (23) Jones, A. L.; Ho, C. H. Y.; Riley, P. R.; Angunawela, I.; Ade, H.; So, F.; Reynolds, J. R. Investigating the active layer thickness dependence of non-fullerene organic solar cells based on PM7 derivatives. *J. Mater. Chem. C* **2020**, *8*, 15459–15469.
- (24) Panzer, F.; Bässler, H.; Köhler, A. Temperature Induced Order–Disorder Transition in Solutions of Conjugated Polymers Probed by Optical Spectroscopy. *J. Phys. Chem. Lett.* **2017**, *8*, 114–125.
- (25) Spano, F. C.; Silva, C. H- and J-Aggregate Behavior in Polymeric Semiconductors. *Annu. Rev. Phys. Chem.* **2014**, *65*, 477–500
- (26) Vezie, M. S.; Few, S.; Meager, I.; Pieridou, G.; Dörling, B.; Ashraf, R. S.; Goñi, A. R.; Bronstein, H.; McCulloch, I.; Hayes, S. C.; et al. Exploring the origin of high optical absorption in conjugated polymers. *Nat. Mater.* **2016**, *15*, 746–753.
- (27) Zhang, M.; Oldenhof, H.; Sydykov, B.; Bigalk, J.; Sieme, H.; Wolkers, W. F. Freeze-drying of mammalian cells using trehalose: preservation of DNA integrity. *Sci. Rep.* **2017**, *7*, 6198.
- (28) Xu, Z.; Park, K. S.; Kwok, J. J.; Lin, O.; Patel, B. B.; Kafle, P.; Davies, D. W.; Chen, Q.; Diao, Y. Not All Aggregates Are Made the Same: Distinct Structures of Solution Aggregates Drastically Modulate Assembly Pathways, Morphology, and Electronic Properties of Conjugated Polymers. *Adv. Mater.* 2022, 34, 2203055.
- (29) Wang, Z.-Y.; Di Virgilio, L.; Yao, Z.-F.; Yu, Z.-D.; Wang, X.-Y.; Zhou, Y.-Y.; Li, Q.-Y.; Lu, Y.; Zou, L.; Wang, H. I.; et al. Correlating Charge Transport Properties of Conjugated Polymers in Solution Aggregates and Thin-Film Aggregates. *Angew. Chem., Int. Ed.* **2021**, 60, 20483–20488.
- (30) Kwok, J. J.; Park, K. S.; Patel, B. B.; Dilmurat, R.; Beljonne, D.; Zuo, X.; Lee, B.; Diao, Y. Understanding Solution State Conformation and Aggregate Structure of Conjugated Polymers via Small Angle X-ray Scattering. *Macromolecules* **2022**, *55*, 4353–4366.

- (31) Park, K. S.; Xue, Z.; Patel, B. B.; An, H.; Kwok, J. J.; Kafle, P.; Chen, Q.; Shukla, D.; Diao, Y. Chiral emergence in multistep hierarchical assembly of achiral conjugated polymers. *Nat. Commun.* **2022**, *13*, 2738.
- (32) Tivol, W. F.; Briegel, A.; Jensen, G. J. An improved cryogen for plunge freezing. *Microsc. Microanal.* **2008**, *14*, 375–379.
- (33) Schmidt, K.; Tassone, C. J.; Niskala, J. R.; Yiu, A. T.; Lee, O. P.; Weiss, T. M.; Wang, C.; Fréchet, J. M.; Beaujuge, P. M.; Toney, M. F. A Mechanistic Understanding of Processing Additive-Induced Efficiency Enhancement in Bulk Heterojunction Organic Solar Cells. Adv. Mater. 2014, 26, 300–305.
- (34) Brady, M. A.; Ku, S.-Y.; Perez, L. A.; Cochran, J. E.; Schmidt, K.; Weiss, T. M.; Toney, M. F.; Ade, H.; Hexemer, A.; Wang, C.; Hawker, C. J.; Kramer, E. J.; Chabinyc, M. L. Role of solution structure in self-assembly of conjugated block copolymer thin films. *Macromolecules* **2016**, *49*, 8187–8197.
- (35) Li, Y.-C.; Chen, K.-B.; Chen, H.-L.; Hsu, C.-S.; Tsao, C.-S.; Chen, J.-H.; Chen, S.-A. Fractal Aggregates of Conjugated Polymer in Solution State. *Langmuir* **2006**, *22*, 11009–11015.
- (36) Li, Y.-C.; Chen, C.-Y.; Chang, Y.-X.; Chuang, P.-Y.; Chen, J.-H.; Chen, H.-L.; Hsu, C.-S.; Ivanov, V. A.; Khalatur, P. G.; Chen, S.-A. Scattering study of the conformational structure and aggregation behavior of a conjugated polymer solution. *Langmuir* **2009**, *25*, 4668–4677
- (37) Koberstein, J. T.; Picot, C.; Benoit, H. Light and neutron scattering studies of excess low-angle scattering in moderately concentrated polystyrene solutions. *Polymer* **1985**, *26*, 673–681.
- (38) Ovchinnikov, Y. K.; Antipov, E. M.; Markova, G. S.; Bakeev, N. F. Comparative investigation of short-range order in unbranched alkanes and polyethylene. *Macromol. Chem. Phys.* **1976**, *177*, 1567–1581.
- (39) Sunday, D. F.; Martin, T. B.; Chang, A. B.; Burns, A. B.; Grubbs, R. H. Addressing the challenges of modeling the scattering from bottlebrush polymers in solution. *J. Polym. Sci.* **2020**, *58*, 988–996
- (40) Pedersen, J. S.; Schurtenberger, P. Scattering functions of semiflexible polymers with and without excluded volume effects. *Macromolecules* **1996**, *29*, 7602–7612.
- (41) Pedersen, J. S. Analysis of small-angle scattering data from colloids and polymer solutions: modeling and least-squares fitting. *Adv. Colloid Interface Sci.* **1997**, *70*, 171–210.
- (42) Abdelsamie, M.; Chaney, T. P.; Yan, H.; Schneider, S. A.; Ayhan, I. A.; Gomez, E. D.; Reynolds, J. R.; Toney, M. F. Revealing temperature-dependent polymer aggregation in solution with small-angle X-ray scattering. *J. Mater. Chem. A* **2022**, *10*, 2096–2104.
- (43) Yao, H.; Ye, L.; Zhang, H.; Li, S.; Zhang, S.; Hou, J. Molecular design of benzodithiophene-based organic photovoltaic materials. *Chem. Rev.* **2016**, *116*, 7397–7457.
- (44) Zheng, B.; Huo, L.; Li, Y. Benzodithiophenedione-based polymers: recent advances in organic photovoltaics. *NPG Asia Mater.* **2020**, *12*, 1–22.
- (45) Chai, J.-D.; Head-Gordon, M. Long-range corrected hybrid density functionals with damped atom—atom dispersion corrections. *Phys. Chem. Chem. Phys.* **2008**, *10*, 6615—6620.
- (46) Chai, J.-D.; Head-Gordon, M. Systematic optimization of longrange corrected hybrid density functionals. *J. Chem. Phys.* **2008**, *128*, No. 084106.
- (47) Körzdörfer, T.; Bredas, J.-L. Organic electronic materials: recent advances in the DFT description of the ground and excited states using tuned range-separated hybrid functionals. *Acc. Chem. Res.* **2014**, *47*, 3284–3291.
- (48) Sutton, C.; Körzdörfer, T.; Gray, M. T.; Brunsfeld, M.; Parrish, R. M.; Sherrill, C. D.; Sears, J. S.; Brédas, J.-L. Accurate description of torsion potentials in conjugated polymers using density functionals with reduced self-interaction error. *J. Chem. Phys.* **2014**, *140*, No. 054310.
- (49) Hestand, N. J.; Spano, F. C. The effect of chain bending on the photophysical properties of conjugated polymers. *J. Phys. Chem. B* **2014**, *118*, 8352–8363.

- (50) Barford, W.; Marcus, M. Perspective: Optical spectroscopy in π -conjugated polymers and how it can be used to determine multiscale polymer structures. *J. Chem. Phys.* **2017**, *146*, 130902.
- (51) Nguyen, T.-Q.; Doan, V.; Schwartz, B. J. Conjugated polymer aggregates in solution: Control of interchain interactions. *J. Chem. Phys.* **1999**, *110*, 4068–4078.
- (52) Zhang, S.; Qin, Y.; Zhu, J.; Hou, J. Over 14% efficiency in polymer solar cells enabled by a chlorinated polymer donor. *Adv. Mater.* **2018**, *30*, 1800868.
- (53) Le Berre, M.; Chen, Y.; Baigl, D. From convective assembly to Landau— Levich deposition of multilayered phospholipid films of controlled thickness. *Langmuir* **2009**, 25, 2554—2557.
- (54) Qu, G.; Kwok, J. J.; Mohammadi, E.; Zhang, F.; Diao, Y. Understanding Film-To-Stripe Transition of Conjugated Polymers Driven by Meniscus Instability. *ACS Appl. Mater. Interfaces* **2018**, *10*, 40692–40701.
- (55) Gu, X.; Shaw, L.; Gu, K.; Toney, M. F.; Bao, Z. The meniscusguided deposition of semiconducting polymers. *Nat. Commun.* **2018**, *9*, 1–16.
- (56) Diao, Y.; Zhou, Y.; Kurosawa, T.; Shaw, L.; Wang, C.; Park, S.; Guo, Y.; Reinspach, J. A.; Gu, K.; Gu, X. Flow-enhanced solution printing of all-polymer solar cells. *Nat. Commun.* **2015**, *6*, 1–10.
- (57) Rivnay, J.; Mannsfeld, S. C. B.; Miller, C. E.; Salleo, A.; Toney, M. F. Quantitative determination of organic semiconductor microstructure from the molecular to device scale. *Chem. Rev.* **2012**, *112*, 5488–5519.
- (58) Baker, J. L.; Jimison, L. H.; Mannsfeld, S.; Volkman, S.; Yin, S.; Subramanian, V.; Salleo, A.; Alivisatos, A. P.; Toney, M. F. Quantification of thin film crystallographic orientation using X-ray diffraction with an area detector. *Langmuir* **2010**, *26*, 9146–9151.
- (59) White, J. L.; Spruiell, J. E. The specification of orientation and its development in polymer processing. *Polym. Eng. Sci.* **1983**, 23, 247–256.
- (60) Zhang, F.; Mohammadi, E.; Qu, G.; Dai, X.; Diao, Y. Orientation-Dependent Host—Dopant Interactions for Manipulating Charge Transport in Conjugated Polymers. *Adv. Mater.* **2020**, *32*, 2002823.
- (61) Collins, B. A.; Gann, E. Resonant soft X-ray scattering in polymer science. *J. Polym. Sci.* **2022**, *60*, 1199–1243.
- (62) Collins, B. A.; Cochran, J. E.; Yan, H.; Gann, E.; Hub, C.; Fink, R.; Wang, C.; Schuettfort, T.; McNeill, C. R.; Chabinyc, M. L.; et al. Polarized X-ray scattering reveals non-crystalline orientational ordering in organic films. *Nat. Mater.* **2012**, *11*, 536–543.
- (63) Ferron, T.; Pope, M.; Collins, B. A. Spectral Analysis for Resonant Soft X-Ray Scattering Enables Measurement of Interfacial Width in 3D Organic Nanostructures. *Phys. Rev. Lett.* **2017**, *119*, No. 167801.
- (64) Watts, B. Calculation of the Kramers-Kronig transform of X-ray spectra by a piecewise Laurent polynomial method. *Opt. Express* **2014**, 22, 23628–23639.
- (65) Debye, P.; Anderson, H. R.; Brumberger, H. Scattering by an Inhomogeneous Solid. II. The Correlation Function and Its Application. *J. Appl. Phys.* **1957**, *28*, 679–683.
- (66) Hu, H.; Chow, P. C. Y.; Zhang, G.; Ma, T.; Liu, J.; Yang, G.; Yan, H. Design of donor polymers with strong temperature-dependent aggregation property for efficient organic photovoltaics. *Acc. Chem. Res.* **2017**, *50*, 2519–2528.
- (67) Park, J. S.; Choi, N.; Lee, C.; Lee, S.; Ha, J.-W.; Hwang, D.-H.; Kim, B. J. Elucidating roles of polymer donor aggregation in all-polymer and non-fullerene small-molecule—polymer solar cells. *Chem. Mater.* **2020**, *32*, 3585—3596.